



## Review

## Design of highly stable and selective core/yolk-shell nanocatalysts—A review

Ziwei Li<sup>a,c,1</sup>, Min Li<sup>b,1</sup>, Zhoufeng Bian<sup>c</sup>, Yasotha Kathiraser<sup>c</sup>, Sibudjing Kawi<sup>c,\*</sup><sup>a</sup> School of Chemical Engineering, Guizhou Institute of Technology, Guiyang 550003, China<sup>b</sup> School of Civil Engineering, Guizhou Institute of Technology, Guiyang 550003, China<sup>c</sup> Department of Chemical and Biomolecular Engineering, National University of Singapore, Singapore 117585, Republic of Singapore

## ARTICLE INFO

## Article history:

Received 26 October 2015

Received in revised form

25 December 2015

Accepted 27 January 2016

Available online 1 February 2016

## Keywords:

Design

Core/yolk shell

Nanocatalysts

Stability

Selectivity

## ABSTRACT

In recent decades, increasing interests have been put on improving the stability and selectivity of nanocatalysts for clean energy production due to the decrease of fossil fuels. Despite the prominent feature of high catalytic activity, nanocatalysts are prone to sintering. Structural design of nanocatalysts to form core/yolk shell structure has been proven to be the most effective method to enhance their catalytic stability. In this review, design strategies for core/yolk shell nanocatalysts to attain high stability in energy related applications at high temperatures such as hydrocarbon reforming reactions for syngas production and high temperature fuel cells such as SOFC and MCFC are summarized and exemplified with the advancements made in the recent three years. In addition, measures taken to obtain outstanding selectivity for F-T synthesis and C=C bond hydrogenation reactions are also presented. Further, excellent shape and size selectivity design examples are also introduced. Finally, unsolved problems and challenges for core/yolk shell nanocatalysts design are proposed as the final part of this review.

© 2016 Elsevier B.V. All rights reserved.

## Contents

1. Introduction .....	325
2. Design principles of sintering resistant property for high temperature clean energy-related applications .....	325
2.1. Syngas production reactions .....	326
2.2. High temperature fuel cells .....	328
2.3. Other high temperature reactions .....	331
2.4. CO oxidation .....	331
2.4.1. Noble metal based core shell nanostructures .....	331
2.4.2. Metal oxide core shell nanostructures .....	332
3. Design of high selectivity .....	333
3.1. F-T synthesis .....	333
3.1.1. H-ZSM-5 zeolite as the shell .....	334
3.1.2. Other zeolites as the shell .....	334
3.2. Selective hydrogenation of acetylenic compounds .....	334
3.3. Other shape and size selectivity design .....	336
3.3.1. Shape selectivity .....	336
3.3.2. Size selectivity .....	337
3.4. Other design examples for high selectivity .....	338

\* Corresponding author.

E-mail address: [chekawis@nus.edu.sg](mailto:chekawis@nus.edu.sg) (S. Kawi).<sup>1</sup> These authors contributed equally to this work.

4. Conclusions and outlook .....	339
Acknowledgements .....	340
Appendix A. Supplementary data .....	340
References .....	340

## 1. Introduction

With the continuous consumption of fossil fuels, alternative energy sources and processes for clean energy production has attracted increasing attention. Almost all these energy production processes are related to catalysis. Continuous endeavors have been made to explore new catalysts especially nanocatalysts with excellent activity, stability and selectivity for clean energy production.

It is well known that catalytic activity will be remarkably increased when the size of catalysts is decreased to nano scale as a result of the greatly increased active sites such as edge and corner atoms [1,2]. Whereas, stability issues of nanomaterials for high temperature reactions such as prone to sintering caused by their high surface energy have to be addressed before they can be employed as catalysts [3]. In addition, selectivity, the rate of a reaction along a particular pathway divided by the sum of rates along all reaction pathways, is one of the most important among the three factors making a good catalyst in addition to activity and stability. The ultimate goal for clean energy production is to achieve 100% selectivity for the desired product for a multipathway reaction while maintaining their activity and stability [4]. To achieve this goal and to efficiently improve the progress for clean energy production, understanding the design principles and the underlining science is important.

Sintering of active metal usually happens when catalysts endure harsh conditions such as high temperature either during catalyst preparation process or under reaction conditions. High temperature (700 °C) is thermodynamically or kinetically required for reactions such as reforming reactions for synthesis gas (syngas) production to achieve economically viable conversions of reactants. In addition, high temperature calcination treatment is normally needed for most catalysts to remove the surfactants which facilitate the synthesis of nanocatalysts but may block their active sites. During these high temperature processes, bonds between atoms and bonds between crystallite and the underlying surface will be broken, leading to the migration and growth of atoms and crystallites [5]. These migrations will result in the increase of particle size, deformation of the shape as well as change of composition and finally catalyst deactivation.

Various methods have been investigated to solve the above problems of nanocatalysts. These methods include: First, embedding nanoparticles inside controlled cavities [6] or channels of the pre-synthesized mesoporous materials such as SBA [7,8] and MCM [9] families, one dimensional metal oxide nanotubes [10] or carbon nanotubes [11,12] as well as within the pores of graphitic spheres [13] and metal organic frame works (MOF) [14]; Second, developing materials with stronger interaction between nanoparticles and support such as perovskite [15,16], spinel [17], hydroxalcite (HT) [18] and layered double hydroxide (LDH) [19] as well as bimetallic alloy nanoparticles supported catalysts [20–22]; Third, constructing core/yolk shell nanostructures by coating the presynthesized nanoparticles with another layer [23–34] or layers of shells [35–38], by one pot synthetic methods [39,40] and by surface-protected etching method [41].

Most of these methods described here have been reviewed by Fornasiero's group [6] and Veszteg's group [5] especially for the first two methods. The references provided above are the progresses made in the recent three years by other groups. As discussed in other studies, the first two methods cannot completely prohibit

the migration and sintering of nanoparticles [42,43]. This illustrates that these two methods cannot effectively eliminate the Ostwald ripening of nanoparticles, resulting in their growth [44]. Therefore, in this review, we will focus on the third method i.e. core/yolk shell nanostructures as active and stable catalysts.

Core/yolk shell nanocatalysts also have been continuously reviewed by different research groups, reflecting the continuing growth of interests in this topic [45–49]. However, most of them are from the materials synthesis aspect [45–48] or focused on either one type of material for instance noble metal based [39] or one type of reaction such as liquid phase reaction [49]. Even though catalytic applications were also summarized, the design principles for these core/yolk shell nanostructures to these applications are not illuminated in detail.

Core/yolk shell nanostructures have been extensively studied and applied in various areas such as catalysts [42] and energy storage materials [50], owing to their flexibility to be functionally designed catering to the specific needs. Take catalysts as an example, the structure of core shell catalysts determines their catalytic performance, as shown in Fig. 1, (1) Active sites can be designed at either the core/shell part or even at the molecules functionalized to the shell surface or at all of these places. For active sites located in the core part and embedded within the shell, the high temperature stability will be enhanced. (2) Shell porosity, the pore size and shell thickness can be finely tuned to attain size selectivity and shape selectivity. (3) Materials of both the core and shell part can be tailored to acquire the best synergetic effect [51]. In addition, multifunctionality such as amphiphilic property [52], acid-base bifunctionality [53] and temperature responsive catalytic property [54] also can be obtained. (4) Core/yolk shell nanostructures can also be combined with other nanostructures such as 1d carbon nanotubes [55] and high surface area oxides [56] to further improve their catalytic performances.

In this review, the synthesis methods and procedures for core/yolk shell nanostructures will not be covered. Instead, based on the design perspectives described above, we report the progresses in designing core/yolk shell catalysts mostly in the recent three years as follows: Firstly, design principles to achieve sinter-resistant property for high temperature energy-related applications such as synthesis gas production reactions and high temperature fuel cells; Although CO oxidation operates at relative low temperatures, it is quite sensitive to the active metal particle size. Therefore, sinter-resistant core shell catalysts including both metal and metal oxides for CO oxidation reaction will also be included. Secondly, methods used to get high catalytic selectivity for reactions such as F-T synthesis reaction and selective hydrogenation reactions for the C–C triple bonds as well as the design examples for size and shape selectivity. For selective hydrogenation reaction, since metals such as Pd exhibits outstanding high selectivity, most of the core shell catalysts will be focused on metals. Finally, the unsolved problems of core/yolk shell nanocatalysts are discussed and the potential future research directions are identified.

## 2. Design principles of sintering resistant property for high temperature clean energy-related applications

To prohibit high temperature sintering, active sites either metal or metal oxide have to be located at the core or embedded

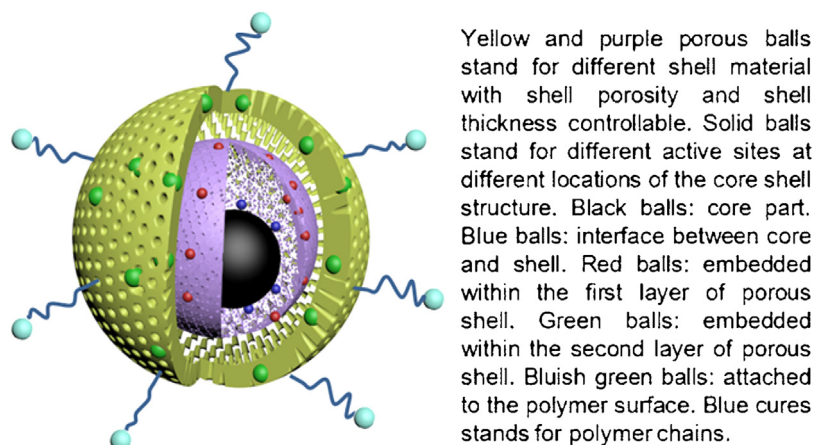


Fig. 1. Schematic illustration of design strategies for core/yolk shell nanocatalysts.

within the shell of core/yolk shell nanostructures. In this way, stronger interaction between active sites and the surrounding shell materials will be achieved, retarding the sintering of active sites. Therefore, carbon resistance and even corrosion resistance can also be achieved. In the following section, sinter-resistant core/yolk shell nanocatalysts for high temperature energy-related applications will be specifically introduced with the emphasis on the design philosophies.

### 2.1. Syngas production reactions

Syngas, a mixture of CO and H<sub>2</sub>, is a critical feedstock for the production of easier transportable liquid fuel energies such as methanol and light olefins as well as value added chemicals such as ammonia and acetic acid [57]. It is produced mainly by reforming reactions such as steam reforming of methane (SRM) [58,59], CO<sub>2</sub> (dry) reforming of methane (DRM) [60,61], partial oxidation of methane (POM) [62] and ethanol steam reforming (ESR) [63,64] as well as a combination of some of these reactions together [65]. Ni based catalysts are preferred for these reforming reactions due to their outstanding catalytic activities and low cost [66]. Whereas, Ni based active nanoparticles within these catalysts tend to grow bigger due to sintering under high temperature reaction conditions, leading to serious carbon deposition which degrades catalytic performance [67–69]. The carbon deposition is a common problem especially for DRM reaction [70]. By forming core/yolk shell structure, sintering of Ni nanoparticles can be eliminated thereby enhancing the carbon resistance property of the Ni based catalysts. This is because it has been reported that carbon deposition preferentially occurs on Ni nanoparticles with big particle size (larger than 9 nm) [71,72]. Examples of these core/yolk shell nanostructures are summarized as follows.

In our group, yolk-satellite-shell structured Ni-yolk@Ni@SiO<sub>2</sub> nanocomposites were developed for DRM reaction to tackle the carbon deposition while maintaining activity and stability [23]. As shown in Fig. 2, sintering prevention of active Ni nanoparticles was achieved by trapping them at the core part and inside the silica shell. The nanocomposite with 11.2 nm shell thickness exhibited the best catalytic performance with the initial CH<sub>4</sub> turn over frequency (TOF) of 85.8 s<sup>-1</sup> at 800 °C. This was higher than Ni/SiO<sub>2</sub>@SiO<sub>2</sub> (8.22 s<sup>-1</sup> at 800 °C) and the supported catalysts Ni-Zr/MCM-41 (1.2 s<sup>-1</sup> at 750 °C) [73], Ni/MCM-41 (0.75 s<sup>-1</sup> at 750 °C) [73], Ni-xCe-Al (1.2 s<sup>-1</sup> at 800 °C) [74] and Ni/MgO (1.5–3.8 s<sup>-1</sup>) [75]. The authors attributed this to its relatively high Ni dispersion and confinement effect (the homogeneous reaction microenvironment where reactants are enriched [76–82]), resulting from

the yolk shell structure. The high Ni dispersion was due to the formation of the satellite nickels which were formed from the decomposition of Ni phyllosilicate (Ni-Phy) species at the interface between Ni and SiO<sub>2</sub> because of their strong interaction. However, it is noted that the specific surface area and Ni exposure of this nanocomposite was not so high, which is not desirable for industrial use in lower temperature reactions.

Following this, specific surface area controllable Ni@Ni embedded SiO<sub>2</sub> yolk shell nanocatalysts were designed by the same group, showing enhanced catalytic activity compared with Ni-yolk@Ni@SiO<sub>2</sub> catalysts (Fig. 3) [25]. The TOF value increased by 2 times and 4.5 times at 800 °C for Ni@Ni embedded SiO<sub>2</sub> catalyst with the treatment duration of 12 h and 24 h respectively compared with Ni@SiO<sub>2</sub> catalyst without treatment. This enhanced catalytic performance was attributed to the higher surface Ni exposure of Ni-phy species which was formed due to the reaction between nickel hydroxide species and silicic acid under basic reaction condition. This Ni@Ni embedded SiO<sub>2</sub> catalyst also exhibited stable reactant conversions at the lower DRM temperature of 700 °C. The improved specific surface area and surface Ni exposure of Ni@Ni embedded SiO<sub>2</sub> catalyst accounted for its improved catalytic performance.

Another core shell catalyst, Nickel@Nickel-Magnesium phyllosilicate (Ni@Ni-MgPhy), was developed by the same group via hydrothermal treatment method to increase the Ni accessibility and the basicity of Ni-yolk@Ni@SiO<sub>2</sub> catalyst (Fig. 4) [24]. By treating Ni@SiO<sub>2</sub> with Mg(NO<sub>3</sub>)<sub>2</sub> salt for different durations, both porosity and basicity can be easily tuned, achieving high Ni exposure and strong basicity thereby high catalytic activity and carbon-resistant property. The TOF for Ni@Ni-MgPhy catalyst with 10 h treatment duration was 3.3 times higher than that of Ni@SiO<sub>2</sub> at 700 °C. This proposed hydrothermal treatment method is promising to synthesize other multifunctional core shell materials.

Du et al. proposed NiMgAl-layered double hydroxide@m-SiO<sub>2</sub> core shell catalyst for DRM (Fig. 5) [83]. Sintering of Ni active metal was prevented by dispersing them in LDH promoted by MgO; while silica shell prevents the sintering of LDH particles. Thus, this synthesis technique resulted in small Ni particle size and high carbon resistance property (further improved with presence of the basic MgO, facilitating CO<sub>2</sub> chemisorption and activation). These led to high catalytic conversions and negligible carbon formation at 750 °C. However, if longer than 8 h duration for stability test could be done to prove its excellent stability in the future, the catalytic results should be more convincing.

Zeng and coworkers synthesized Mg-Al-Ni hydrotalcite with a Ni rich shell-core structure catalyst for ESR reaction with the aim of



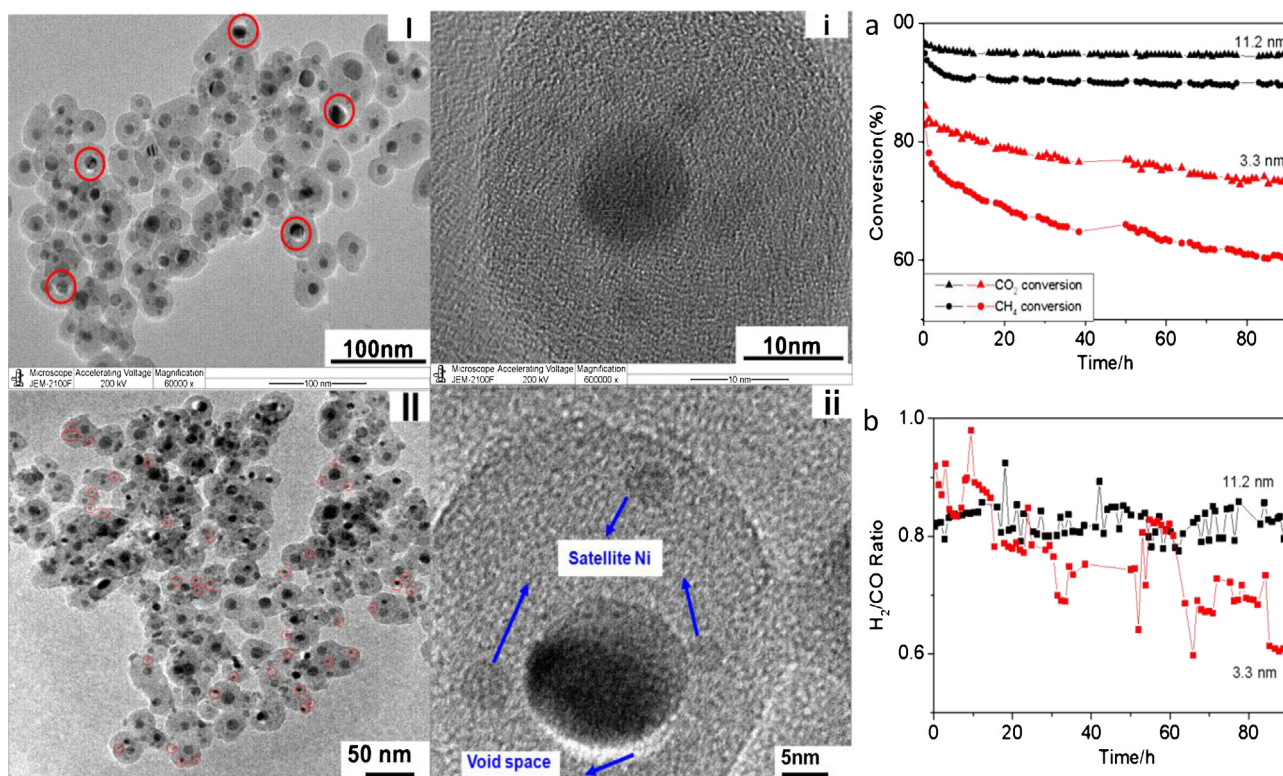


**Fig. 2.** TEM images of Ni-yolk@Ni@SiO<sub>2</sub> with 11.2 nm shell thicknesses: I and (i) After reduction under H<sub>2</sub> at 800 °C for 2 h, II and (ii) after reaction at 800 °C for 20 h; a and b) Stability test for Ni@SiO<sub>2</sub> with 3.3 nm shell thickness and Ni-yolk@Ni@SiO<sub>2</sub> with 11.2 nm shell thickness. Conditions: 800 °C, GHSV = 36,000 mL g<sup>-1</sup> cat h<sup>-1</sup>, CO<sub>2</sub>:CH<sub>4</sub>:N<sub>2</sub> = 1:1:1. Reprinted with permission from ref [23], copyright (2014) American Chemical Society.

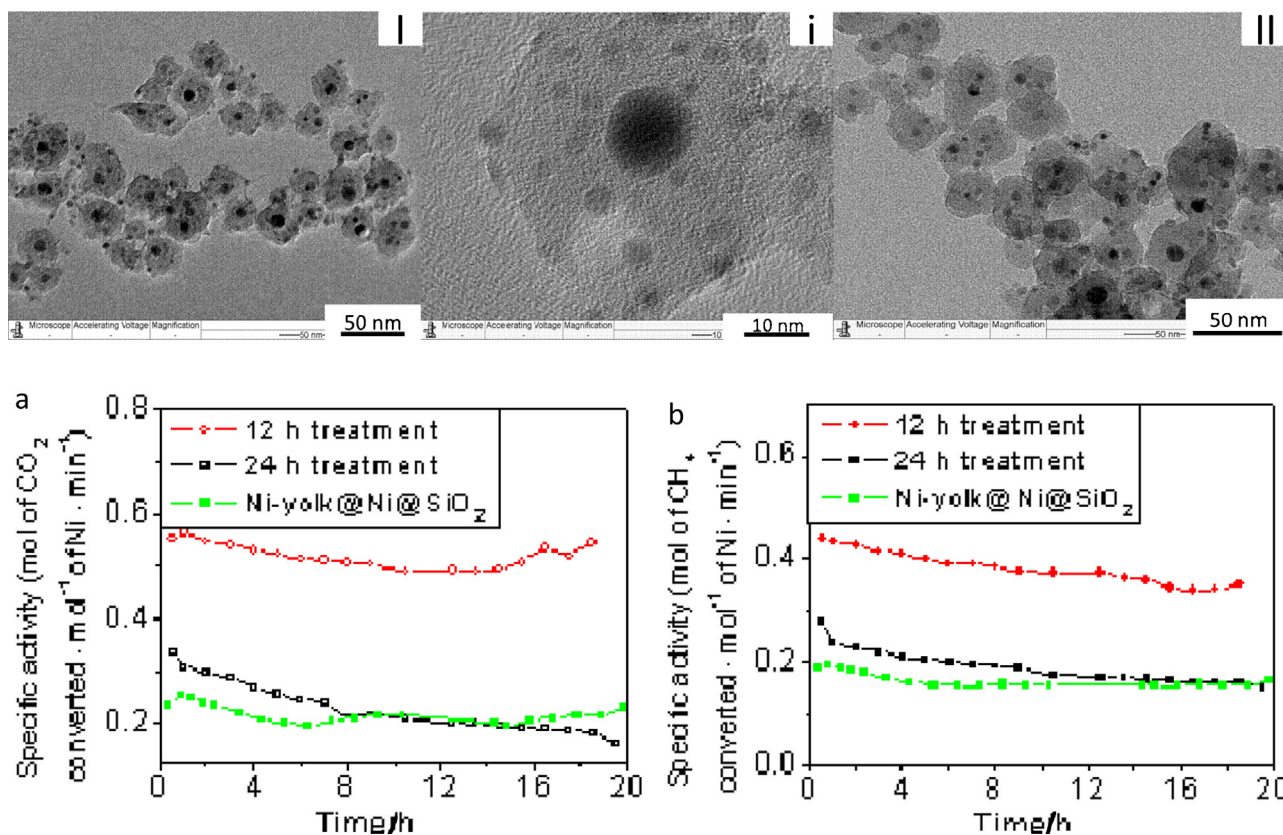


**Fig. 3.** TEM images for Ni@Ni embedded SiO<sub>2</sub> yolk shell nanocomposites with the treatment of 12 h: (I) and (i) before reaction, (II) after reaction for 20 h. (a) and (b) Specific activity for Ni@Ni embedded SiO<sub>2</sub> yolk shell nanocomposite with different treatment duration and Ni-yolk@Ni@SiO<sub>2</sub> nanocomposite after calcination at 800 °C, reaction conditions: 800 °C, GHSV = 1440 L g<sup>-1</sup> cat h<sup>-1</sup>, W<sub>cat</sub> = 0.01 g, CO<sub>2</sub>:CH<sub>4</sub>:N<sub>2</sub> = 1:1:1. Reprinted with permission from ref [25], copyright (2015) John Wiley and Sons.

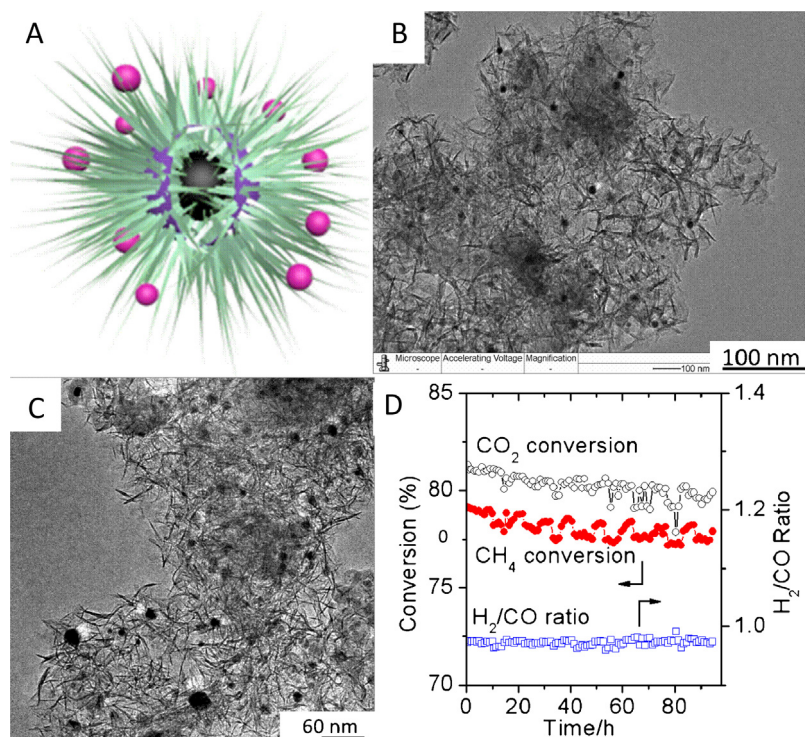


**Fig. 4.** Schematic drawing (A), TEM images (B–C) and stability test (D) for Ni@Ni-Mg phyllosilicate core shell catalyst after treatment for 10 h: (B) before reaction and (C) after reaction. Conditions: 700 °C, Wcat = 0.05 g, GHSV = 36 L g<sup>−1</sup> cat h<sup>−1</sup>, CO<sub>2</sub>:CH<sub>4</sub>:N<sub>2</sub> = 1:1:1. Reprinted with permission from Ref. [24], copyright (2014) American Chemical Society.

improving the Ni accessibility, reducibility and dispersion [84]. This was realized by a dense flake-like Ni rich sheets film which was constituted in the outer layer of Mg–Al–Ni HT, preventing the further penetration of Ni<sup>2+</sup> ions into its bulk. The catalyst with the lowest Ni content exhibited the highest H<sub>2</sub> yield at 700 °C without observable drop in activity even after 50 h. This H<sub>2</sub> yield (mol/(mol ethanol•mol total Ni)) for the core shell catalyst was estimated to be around 1.7 times higher than the hydrotalcite catalyst NiMg<sub>4</sub>Zn<sub>1</sub>Al [85]. However, the catalyst exhibited slightly high carbon deposition based on thermogravimetric analysis.

Au and Ji's group designed Ni@SiO<sub>2</sub> core shell catalyst with Ni core size and porosity tunable for POM reaction [86]. Catalyst with 6 nm Ni core and 3–4 nm mesopores in the shell exhibited the best CH<sub>4</sub> conversion with highest H<sub>2</sub> selectivity at 750 °C. As discussed in the manuscript, this catalyst showed notably better activity and stability than the conventional supported catalyst Ni/SiO<sub>2</sub>, Ni/γ-Al<sub>2</sub>O<sub>3</sub> [87], Ni supported on Al<sub>2</sub>O<sub>3</sub> modified by aluminum phosphate [87] and Li<sub>2</sub>O- and La<sub>2</sub>O<sub>3</sub>-doped Ni/Al<sub>2</sub>O<sub>3</sub> catalysts [88]. However, the authors observed Ni metal sintering which was attributed to the trapping of multi Ni nanoparticles inside one SiO<sub>2</sub> shell. If the catalysts preparation techniques could be improved, the catalytic performance should be better.

Recently, a redox catalyst, Fe<sub>2</sub>O<sub>3</sub>@La<sub>x</sub>Sr<sub>1-x</sub>FeO<sub>3</sub>, was designed for POM reaction performed via the chemical looping reforming process (Fig. 6) [89]. This catalyst combined the advantage of high oxygen donor ability of Fe<sub>2</sub>O<sub>3</sub> and the advantage of excellent syngas selectivity of La<sub>x</sub>Sr<sub>1-x</sub>FeO<sub>3</sub> perovskite. By forming core shell structure, with Fe<sub>2</sub>O<sub>3</sub> redox material as the core, sintering of Fe<sub>2</sub>O<sub>3</sub> was refrained, leading to more availability of lattice oxygen. The accessibility of the lattice oxygen by the reactant gases was promoted by the conductive perovskite shell. In addition, the well-defined perovskite shell surface ensured the high syngas selectivity. The carbon formation was inhibited due to the coverage of metallic Fe by the perovskite shell. This core shell redox catalyst showed 10–200 times more activity than the inert and yttria-stabilized

zirconia-supported redox catalysts. In addition, its reactivity can be maintained even after more 100 redox cycles at 900 °C, showing excellent stability which is encouraging and promising for industrial application.

Kang and coworkers synthesized and applied Al<sub>2</sub>O<sub>3</sub>-Ni and MgO-Al<sub>2</sub>O<sub>3</sub>-Ni core shell catalysts to mixed reforming of methane (MRM, ie. combination of SRM and DRM) reaction and autothermal reforming (ATR) reaction [90]. The well dispersed NiO and NiOx species shell on the oxide support core formed strong interaction with Ni<sup>2+</sup> ions in the interface between the core and shell, thus prohibiting sintering process and carbon formation. Under the same reaction conditions, Al<sub>2</sub>O<sub>3</sub>-Ni and MgO-Al<sub>2</sub>O<sub>3</sub>-Ni core shell catalysts showed much higher activity and stability for MRM and ATR reactions than the supported Ni catalysts prepared by the precipitation method. However, for the core shell catalysts, the MRM reaction resulted in higher carbon deposition compared to the ATR process due to the carbon-rich environment of the reactants. Nevertheless, as stated by the authors, the specific reasons for the contributions of core shell structure have not been fully understood yet.

## 2.2. High temperature fuel cells

Fuel cell is a device which converts chemical fuel energy to electrical and heat energy. It has high energy conversion efficiency and is environmentally acceptable due to its low emission of gases such as NO<sub>x</sub> and CO<sub>2</sub> [91]. The energy utilization efficiency for high temperature fuel cells such as solid oxide fuel cell (SOFC) [92] and molten carbonate fuel cell (MCFC) [93] are even higher since the waste heat can be recycled to make additional electricity. In addition, hydrocarbon gases such as CH<sub>4</sub> instead of H<sub>2</sub> also can be used as the fuel when the cells are operated as, for example, direct internal reforming molten carbonate fuel cell (DIR-MCFC) [94]. However, the high temperature operating condition of SOFC and DIR-MCFC will lead to the sintering of electrode catalyst and



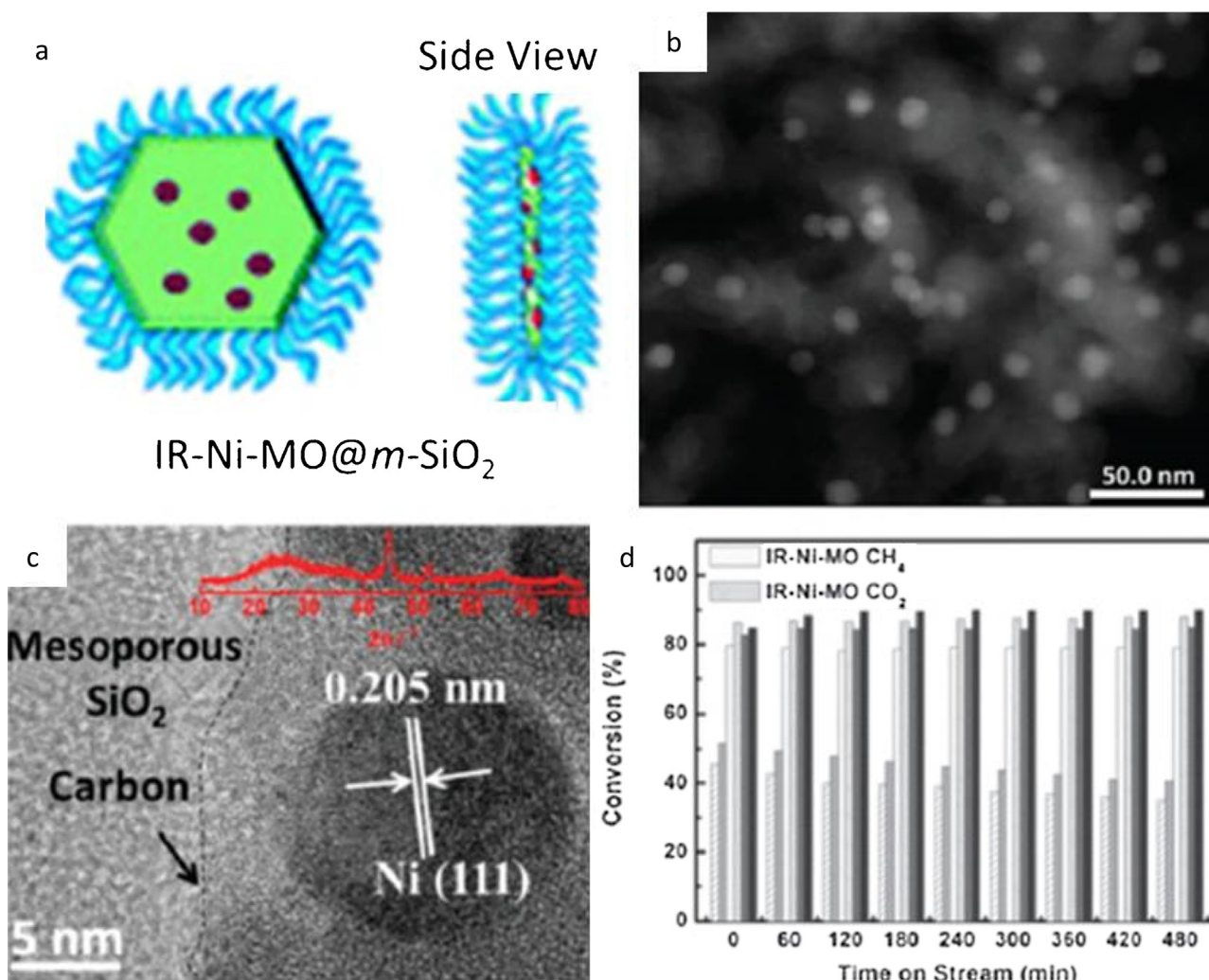


**Fig. 5.** NiMgAl-LDH@m-SiO<sub>2</sub> modular catalysts: (a) Schematic drawing, (b) HAADF-STEM image, (c) HRTEM image for the used catalyst, (d) stability test at 750 °C. Reprinted with permission from Ref. [83], copyright (2013) Royal Society of Chemistry.

thereby the decrease of cell performance. In addition, the reforming catalyst also tends to be poisoned by alkali electrolyte in the DIR-MCFC. Examples of designing highly active and stable high temperature fuel cell catalysts are provided as below.

Vohs's group designed an extremely sinter-resistant SOFC catalyst by depositing a submonolayer of core shell Pd@CeO<sub>2</sub> onto porous YSZ anodes (Fig. 7) [95]. CeO<sub>2</sub> shell alleviated the sintering of Pd during the infiltration process. Meanwhile sintering of Pd@CeO<sub>2</sub> core shell nanoparticles during the high temperature (1123 K) calcination process was prevented by sticking a submonolayer of Pd@CeO<sub>2</sub> to the surface of YSZ through functionalizing the surface with triethoxy(octyl) silane to reduce the surface hydrophobicity. The catalysts exhibited outstanding stability in terms of cell performances compared with uncoated Pd nanoparticles. For cell operating with humidified H<sub>2</sub> fuel at 973 K, when the calcination temperature increased from 723 K to 1123 K, the maximum power density and anode specific resistance remained around 0.3 W cm<sup>-2</sup> and 0.5 Ω m<sup>2</sup> respectively for Pd@CeO<sub>2</sub> catalyst. By comparison, for the uncoated Pd catalyst, a 36% decrease in maximum power density and a 260% increase in anode specific resistance were observed. Moreover, when Pd and Pd@CeO<sub>2</sub>/LSCM/YSZ electrodes were applied to cells with CH<sub>4</sub> as fuel at 973 K, there is a 40% decrease of maximum power density for Pd electrodes, whereas only 9% decrease was observed for Pd@CeO<sub>2</sub> catalyst. In addition, the Pd weight loadings used were as low as 0.001% which greatly

reduced the cost of SOFC. These results showed the promising future for the core shell catalysts to be used for SOFC in terms of both low cost and long lifetime.

Mesoporous MSU-1 shell with large, interconnected mesopores was deposited on Ni/Al<sub>2</sub>O<sub>3</sub> core in order to enhance the transport efficiency of micro-porous Sil-1 without decreasing the alkali-resistant property [96]. A thin Sil-1 layer was deposited on Ni/Al<sub>2</sub>O<sub>3</sub> and acted as a linker surface which was rich in hydroxyl groups for the nucleation and growth of MSU-1. Under the alkali vapor reaction condition, the bare Ni/Al<sub>2</sub>O<sub>3</sub> catalyst without the shell was completely poisoned and is inactive. By comparison, the catalyst with the MSU-1 shell thickness of 10.7 μm exhibited stable activity for 100 h for SRM at the same conditions of DIR-MCFC. However, even though the mesoporous MSU-1 shell improved the CH<sub>4</sub> conversion, compared with the Sil-1 shell with the shell thickness of 3.5 μm catalyst, its stability decreased. In addition, they adopted the traditional impregnation method with few steps of calcination for the Ni species, which could result in the formation of inactive NiAl<sub>2</sub>O<sub>4</sub> phases, leading to decrease of the catalytic performance.

Wang et al. tested the Ni/Al<sub>2</sub>O<sub>3</sub> core Sil-1 shell catalyst prepared by the above group in both unit cell and short stack cells of DIR-MCFC [97]. It was found in the single cell test that the cell voltage increased with the increase of reactive anode gas pressure due to the favored mass transfer and electrode reactions. The 100 h durability test for unit cell yielded a stable average cell voltage of 0.789 V

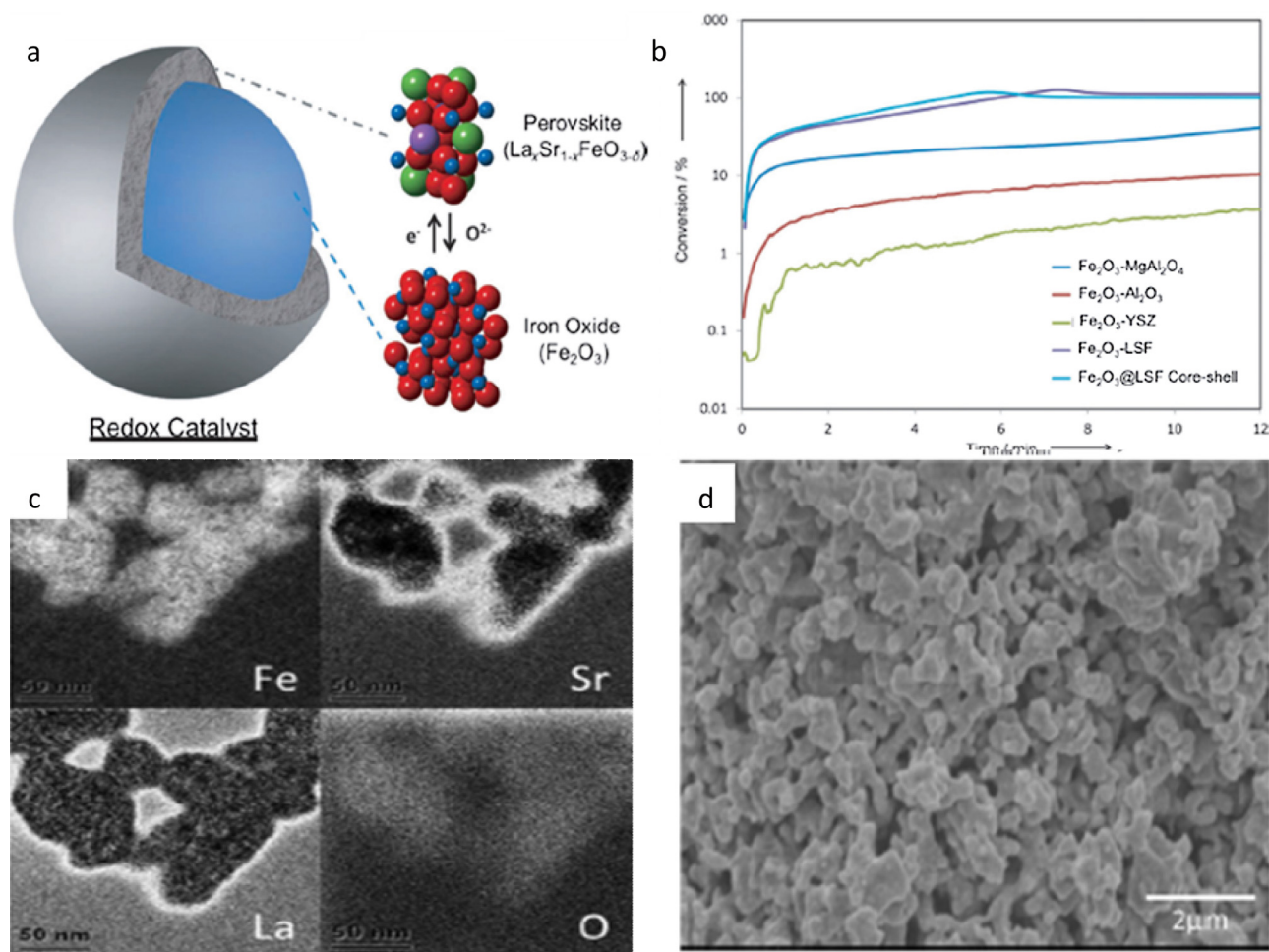


**Fig. 6.** (a) Schematic drawing of  $\text{Fe}_2\text{O}_3\text{@La}_x\text{Sr}_{1-x}\text{FeO}_3$  core-shell redox catalyst; (b) Conversion rates of different redox catalysts in their second cycle reduction in methane; (c) EFTEM mappings of individual elements of  $\text{Fe}_2\text{O}_3\text{@La}_x\text{Sr}_{1-x}\text{FeO}_3$ ; (d) SEM images of the oxidized core-shell particle after 100 cycles. Reprinted with permission from Ref. [89], copyright (2014) John Wiley and Sons.

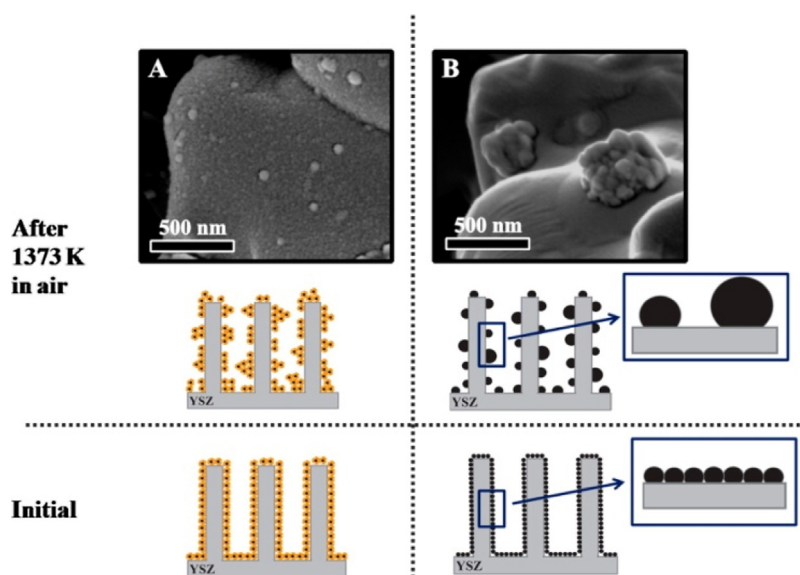


**Fig. 7.** SEM images, with the schematic representation of the agglomeration of  $\text{Pd@CeO}_2$  (panel A) and 2 nm uncoated Pd (panel B) nanoparticles deposited on silanated YSZ porous electrode after samples calcined at 1373 K in air. Reprinted with permission from Ref. [95], copyright (2013) American Chemical Society.

after the decreasing and increasing stages because of the change of the matrix structure and the slight alkali-poisoning in the initial 20 h. The short stack performance also increased with the increase of reactive gases pressure with the maximal output power density of  $338.4 \text{ mW cm}^{-2}$ .

### 2.3. Other high temperature reactions

Cargnello et al. homogeneously deposited Pd@CeO<sub>2</sub> core shell nanoparticles onto the modified hydrophobic Al<sub>2</sub>O<sub>3</sub> (Pd@CeO<sub>2</sub>/H-Al<sub>2</sub>O<sub>3</sub>) (Fig. 8), showing outstanding thermal stability and activity for CH<sub>4</sub> oxidation reaction [98]. In this supported catalyst, sintering of small Pd crystallites was prevented by the CeO<sub>2</sub> shell. Meanwhile the hydrophobic H-Al<sub>2</sub>O<sub>3</sub> support strongly interacted with Pd@CeO<sub>2</sub>, preventing their sintering and altered the oxygen mobility of CeO<sub>2</sub> by the mechanical stress. This helped the stabilization of active PdO<sub>x</sub> phase for CH<sub>4</sub> oxidation reaction, resulting in the outstanding catalytic performance. The reaction rates on Pd@CeO<sub>2</sub>/H-Al<sub>2</sub>O<sub>3</sub> were about 40 times and 200 times higher respectively than the catalysts prepared using incipient wetness impregnation method and impregnation method. This study paved the way for designing high temperature sinter-resistant heterogeneous catalyst.

Another novel core shell nanocomposites synthesized by the same group is the multiwalled carbon nanotubes (MWCNTs) covered by Pt/Pd@oxide (TiO<sub>2</sub>, ZrO<sub>2</sub> and CeO<sub>2</sub>) core shell nanoparticles [99]. Among these core shell catalysts, MWCNTs@ceria/Pd and MWCNTs@ceria/Pt were tested for water gas shift reaction, showing higher activity compared with Pd@CeO<sub>2</sub> and Pt@CeO<sub>2</sub> core shell nanoparticles without MWCNTs. These two nanocomposites also demonstrated outstanding thermal stability even after accelerated aging. These nanocomposites combined the high surface area MWCNTs, highly active nanoparticles Pt/Pd and the high temperature stability of the core shell structure. The high surface area of MWCNTs organized the Pt/Pd@CeO<sub>2</sub> core shell nanoparticles and made the easy accessibility of Pt/Pd active sites which activated the CO reactant gas. This design idea can be a general and promising method to develop other multifunctional nanocomposites by combining other one dimensional nanotubes with the core shell catalysts.

### 2.4. CO oxidation

Catalytic oxidation of CO has attracted enormous attention because it is an important process in removing CO from the automobile exhaust to reduce air pollution [100], prototypical reaction to explore heterogeneous catalysis [101] and H<sub>2</sub> purification for PEMFC [102]. Noble metals such as Pt [103], Pd [104] and Au [105] showed highly active performance for CO oxidation since these metals had strong adsorption ability toward CO. Even though CO oxidation usually runs at low temperatures, the catalyst activity is very sensitive to the particle size of active metal. In addition, CO oxidation usually displays ignition behavior [106]. Regarding these, core shell structure has been widely used to maintain the particle size of noble metals and improve its long-term stability for CO oxidation. In addition to noble metals, transition metal oxides such as CeO<sub>2</sub> [107], Co<sub>3</sub>O<sub>4</sub> [108] and TiO<sub>2</sub> [109] also exhibited promising activity toward CO oxidation due to their outstanding property for O<sub>2</sub> adsorption and activation. In the following, examples of both these two kinds of catalysts with core shell structure will be summarized.

#### 2.4.1. Noble metal based core shell nanostructures

High temperature sinter-resistant core shell nanocomposite SiO<sub>2</sub>@TiO<sub>2</sub>@Au@SiO<sub>2</sub> with Au embedded at the interface of TiO<sub>2</sub> and the outermost mesoporous SiO<sub>2</sub> shell layers was designed by

Zhang et al. for CO oxidation reaction [35]. With the protection of the outermost SiO<sub>2</sub> shell, the size of Au nanoparticles deposited on the TiO<sub>2</sub> surface did not change so much after calcination at 500 °C for 4 h. By comparison, SiO<sub>2</sub>@TiO<sub>2</sub>@Au sample without the outermost SiO<sub>2</sub> layer, Au size increased by 2.5 times. In addition, the outermost SiO<sub>2</sub> shell also hindered the phase transformation of TiO<sub>2</sub> from amorphous to anatase, promoting the formation of well-dispersed small grain size crystal on the SiO<sub>2</sub> surface. These small TiO<sub>2</sub> crystals greatly improved the CO oxidation activity not only because they can provide reactive oxygen owing to their reducibility but also because they helped the dispersion of Au nanoparticles aided by the strong interactions between them. Furthermore, etching of the outermost dense SiO<sub>2</sub> layer to generate mesopores further enhanced the mass transport efficiency for the reaction, resulting in complete conversion at 50 °C.

Li's group synthesized Pd@SiO<sub>2</sub> core shell catalyst with outstanding stability and activity for CO oxidation reaction after calcination at 873 K for 4 h [110]. The reaction rate for Pd@SiO<sub>2</sub> core shell structure was considerably higher ( $22.4 \text{ mmol}_{\text{CO}} \text{ mol}_{\text{Pd}}^{-1} \text{ s}^{-1}$ ) than that of supported Pd/SiO<sub>2</sub> catalyst ( $0.81 \text{ mmol}_{\text{CO}} \text{ mol}_{\text{Pd}}^{-1} \text{ s}^{-1}$ ). In addition, Pd@SiO<sub>2</sub> core shell structure also exhibited a lower light-off temperature (403 K) compared to the supported catalyst. The authors attributed the high catalytic activity to the small Pd size maintained by the SiO<sub>2</sub> shell compared with the severe sintering of Pd for the supported catalyst. These small Pd nanoparticles weakened the adsorption strength of CO, leaving more active sites for O<sub>2</sub> activation which is the rate determine step for CO oxidation. Therefore, more active oxygen atoms were involved in CO oxidation, increasing the catalytic activity. The sinter-resistant property of SiO<sub>2</sub> shell was further demonstrated by the stability test for CO oxidation at 443 K for 576 h with consistent complete CO conversion. However, if the number of empty SiO<sub>2</sub> spheres without Pd within the core can be decreased during the preparation of Pd@SiO<sub>2</sub> core shell catalyst, the catalytic efficiency would be greatly increased.

Active and stable Pt (15 nm)@CeO<sub>2</sub> core shell catalyst was prepared and tested for CO oxidation reaction by Gong's group (Fig. 9) [43]. 50% CO conversion was achieved at around 180 °C with the ignition temperature of 150 °C. The high oxygen storage ability and increased perimeter interface between Pt and CeO<sub>2</sub> due to the formation of core shell structure were attributed to the outstanding catalytic performance. Stable complete conversion of CO was found within the testing period of 50 h at 250 °C and maintained for another 35 h even after annealing at 700 °C for 2 h, suggesting the high sinter-resistant property of this catalyst. By comparison, although Pt@SiO<sub>2</sub>@CeO<sub>2</sub> catalyst has a similar ignition with that of Pt@CeO<sub>2</sub>, the temperature to achieve 50% CO conversion for Pt@SiO<sub>2</sub>@CeO<sub>2</sub> was about 60 °C higher than that of Pt@CeO<sub>2</sub>. However, if the role of oxygen storage ability in improving the catalyst activity could be studied further, a full understanding of the catalytic performance for this core shell catalysts could be obtained.

Another new type core shell structure catalyst with multiple Pt as the core and CeO<sub>2</sub> as the shell was prepared by Wang et al. and tested for CO oxidation reaction [111]. The core shell catalyst showed good structural stability after calcination and lower temperature for complete CO conversion (Fig. 10A and B) compared with the physical mixture of Pt and CeO<sub>2</sub>. The authors attributed to this higher activity of core shell catalysts to the stronger synergistic effect between Pt and CeO<sub>2</sub> due to their closer contact in the core shell structure compared with that in the physical mixture. Calcination decreased the activity of both core shell catalysts and the physical mixture catalysts but this effect was more obviously for the latter (Fig. 10C). A good catalytic stability was found for sample 3 even after 5 reaction cycles (Fig. 10D). This study provided a new synthesis method for the multiple core shell structure catalyst for intermediate high temperature application.



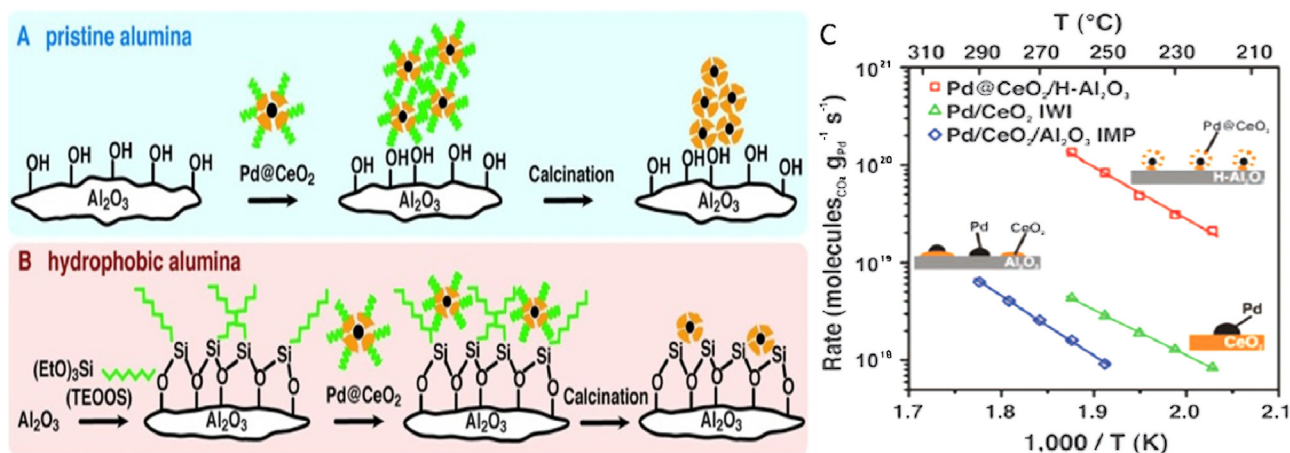


**Fig. 8.** Schematic representation of the agglomeration of  $\text{Pd@CeO}_2$  structures when using the pristine alumina A) and their deposition as single units after treatment of the same support with triethoxy(octyl) silane (TEOS) B); C) Kinetic rate data for  $\text{CH}_4$  oxidation on  $\text{Pd@CeO}_2/\text{H-Al}_2\text{O}_3$  core-shell catalyst,  $\text{Pd/CeO}_2/\text{IWI}$ , and  $\text{Pd/CeO}_2/\text{Al}_2\text{O}_3$ -IMP. Reprinted with permission from Ref. [98], copyright (2012) The American Association for the Advancement of Science.

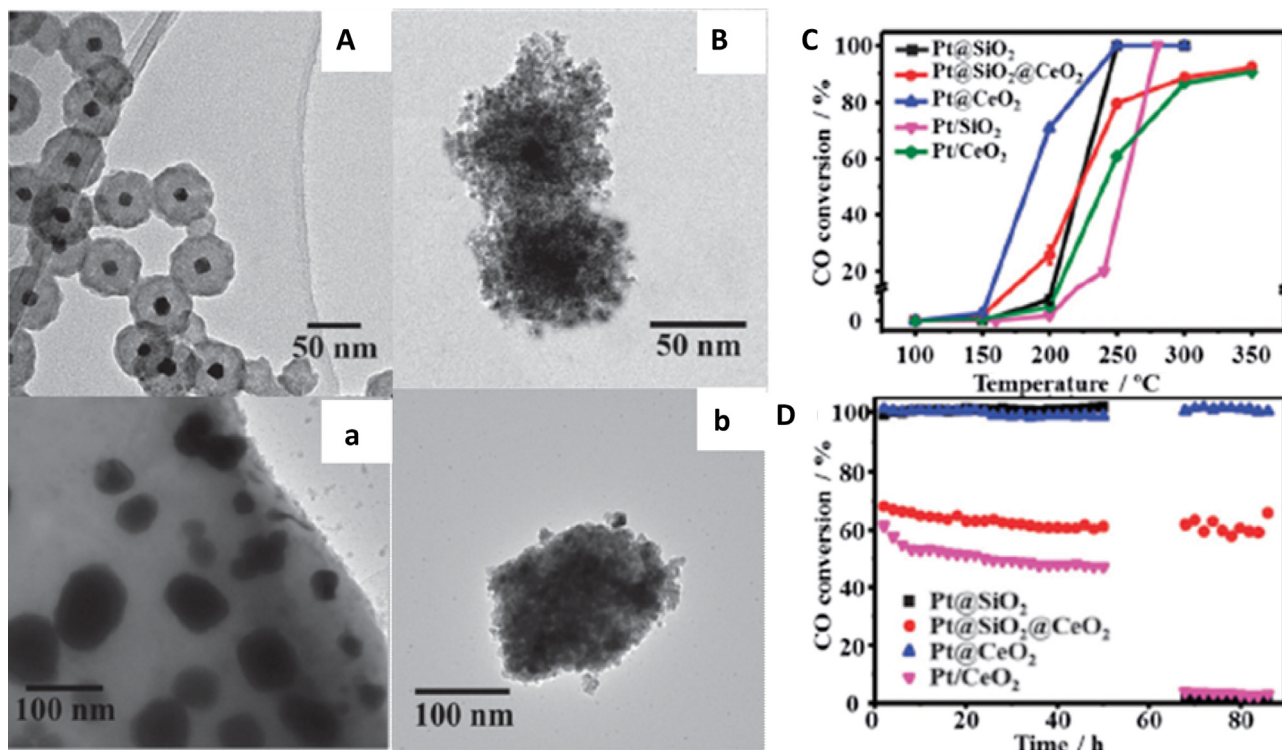


**Fig. 9.** TEM images of (A, B) as-prepared catalysts and (a, b) catalysts after stability test. (A and a)  $\text{Pt@SiO}_2$ , B and (b)  $\text{Pt@CeO}_2$ . (C and D) CO oxidation activity and stability results. Reprinted with permission from Ref. [43], copyright (2013) Royal Society of Chemistry.

#### 2.4.2. Metal oxide core shell nanostructures

Sun and coworkers prepared hollow  $\text{CeO}_2/\text{SiO}_2$  spheres (HCSs) and hollow core/shell  $\text{CeO}_2/\text{SiO}_2/\text{CeO}_2$  spheres (HCCSs) for CO oxidation [112]. HCCSs and HCSs showed CO conversions of 93.7% and 49.7% respectively at 540  $^\circ\text{C}$ . The authors attributed the better catalytic activity of HCCSs to its availability of more active sites due to its higher surface area and the availability of more edge and corner atoms. The phenomena observed in the hollow core shell catalyst preparation process are interesting. However, if direct experimental evidence could be provided, these explanations would be more convincing.

$\text{Co}_3\text{O}_4/\text{CeO}_2$  core shell nanocubes with different shell thickness were synthesized by Zhen et al. and showed excellent activity and stability for CO oxidation [113]. The optimal shell thickness with the

$\text{CeO}_2$  theoretical content of 40 mol% had a complete CO conversion at 190  $^\circ\text{C}$  and maintained at this temperature even after 10 successive cycles from 50 to 250  $^\circ\text{C}$ . Synergetic effect between  $\text{Co}_3\text{O}_4$  and  $\text{CeO}_2$  was enhanced by forming core shell structure as a result of the increase of interfacial area. This synergetic effect brought about its outstanding performance. Unfortunately, there is some information lacking on the exact information of shell thicknesses for these samples as this is a very crucial parameter which determines the extent of catalytic activity.

Surface clean cubic  $\text{Co}_3\text{O}_4/\text{SiO}_2$  yolk shell nanocatalyst was prepared by Yan et al. via an *in situ* decomposition method [114]. The catalyst showed a light off temperature of 120  $^\circ\text{C}$  and a 100% CO conversion at 150  $^\circ\text{C}$ . The clean surface of  $\text{Co}_3\text{O}_4$  enhanced its oxygen donation ability to the surface adsorption of CO to become  $\text{CO}_2$ .

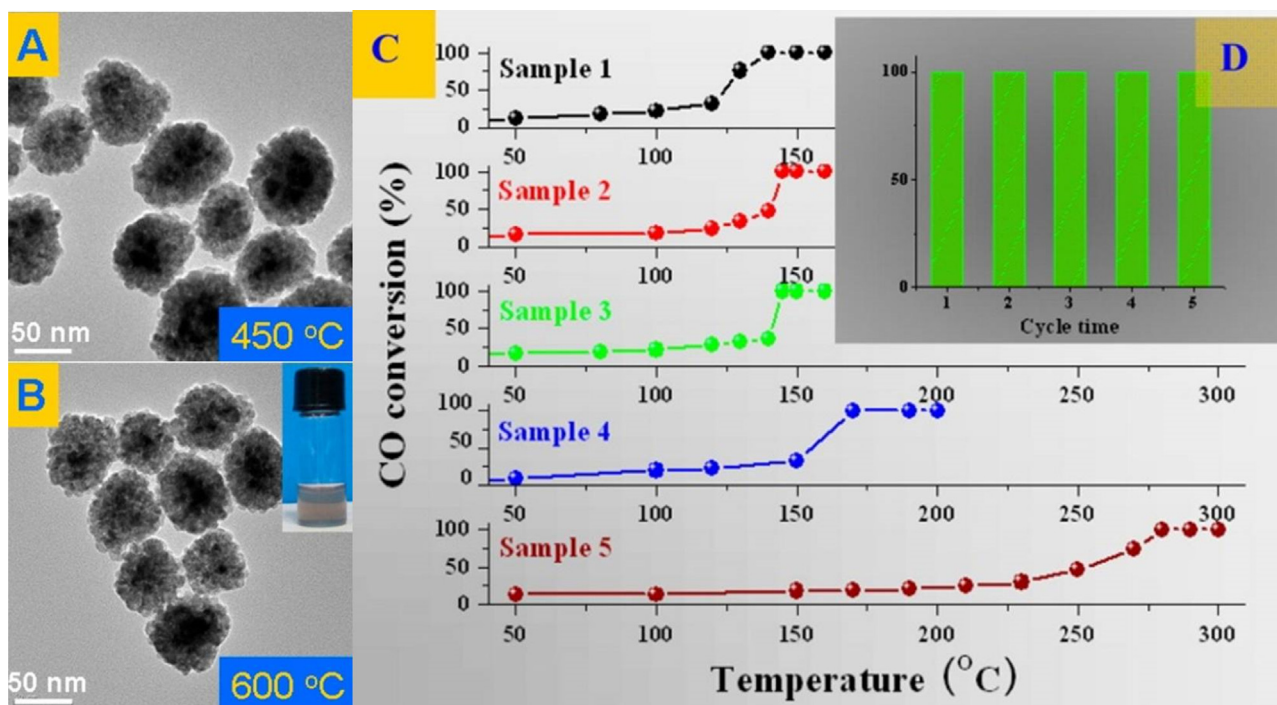


**Fig. 10.** TEM images of (A) sample 2 and (B) sample 3. (C) CO conversion curves of samples 1–5. (D) Catalytic cycles of sample 3 at 150 °C. Sample 1: as synthesized Pt@CeO<sub>2</sub>. Sample 2: calcine sample 1 at 450 °C for 5 h. Sample 3: calcine sample 1 at 600 °C for 5 h. Sample 4: mixture of Pt nanoparticles and CeO<sub>2</sub>. Sample 5: calcine sample 4 at 600 °C for 5 h. Reprinted with permission from ref [111], copyright (2013) American Chemical Society.

The oxygen vacancy formed due to oxygen donation facilitated the adsorption of O<sub>2</sub>. In addition, yolk shell structure provides a nanoreactor (which provides a relatively homogeneous surrounding environment [78–80,115]) for the O<sub>2</sub> and CO to take reaction. All these factors contributed to its excellent catalytic activity.

Another type of oxide core shell catalyst, Al<sub>2</sub>O<sub>3</sub>@CuO with different CuO weight content were synthesized by Chen et al. for CO oxidation via a facile solvothermal strategy [116]. This method avoided the high temperature calcination process thereby eliminating the formation of passive Cu<sub>2</sub>AlO<sub>4</sub> species in the core shell catalyst. In addition, sintering of CuO active species was also alleviated. The temperature for 100% CO conversion decreased with the increase of CuO content with the optimal weight content of 50%. Further increase of CuO weight caused blockage of sites for both CO adsorption and CO<sub>2</sub> desorption, thus requiring higher temperatures for 100% CO conversion. At the same CuO content, core shell catalyst exhibited a lower temperature for 100% CO conversion compared with supported catalyst CuO/Al<sub>2</sub>O<sub>3</sub>. 100 h stability test at 160 °C showed no deactivation of the 50% Al<sub>2</sub>O<sub>3</sub>@CuO catalyst. Unfortunately, as revealed in the paper, this catalyst was not suitable for high temperature reactions because the catalytic active sites which are located on the shell will be sintered.

### 3. Design of high selectivity

The concept of shape or size selectivity is described as: reactants are selectively transformed into products depending on how the processed reactants fit the active site of the catalyst [117,118]. High selectivity is vital because the undesired side reactions can be suppressed and the yield of the target compound can be increased. Specifically, for chemoselectivity, this means that a given functional group can be selectively transformed while other functionalities which are prone to be transformed under the same reaction conditions must be retained. Shape selectivity can be achieved either by poisoning or covering some active sites for the unwanted reactions or by promoting the reaction intermediate which is exclusively

active for certain functionality. Whereas size selectivity is normally realized by controlling the catalyst pore size through which molecules with suitable sizes can pass and reach the active centers. In the following section, design ideas of core shell nanostructures for shape and size selective reactions will be demonstrated.

#### 3.1. F-T synthesis

The Fischer–Tropsch (F-T) synthesis is a vital process to convert syngas (CO + H<sub>2</sub>) into a wide range of long chain hydrocarbons and clean transportation fuels and chemicals without the contamination of sulphur, nitrogen and aromatics [119]. However, it is known that its products follow the Anderson–Schultz–Flory (ASF) rule with a wide carbon number distribution [120]. Therefore, considerable strategies have been taken to improve the catalyst selectivity to the desired product and suppress of byproducts, for example, to maximize lower olefins selectivity but reduce the production of CH<sub>4</sub> and excess CO<sub>2</sub> [121]. These strategies include regulating the diffusion rate of both reactants and products to the active sites, tailoring the particle size of the active metal and modulating the secondary reactions such as hydrogenation, isomerization and hydroformylation. By forming core shell structure with active metal (Fe/Co) as the core and zeolite (H-ZSM-5, SiO<sub>2</sub>, H-Mordenite) as the shell, high selectivity of shorter chain hydrocarbons can be achieved due to the different diffusion rate of reactants within the pores of zeolite shell. This resulted in H<sub>2</sub>-rich conditions near Fe/Co active sites thereby increasing the chain termination probability. In addition, the collision possibility between linear hydrocarbons and active acidic sites was greatly improved. All of these lead to the high selectivity of lighter hydrocarbons. Therefore, core shell structure can be utilized to improve the catalyst selectivity by tuning the shell porosity and shell thickness, adjusting and maintaining the active metal particle size with shell protection and maximizing the synergy effect between the active metal and shell material. The design of these core shell structures are summarized as follows.

### 3.1.1. H-ZSM-5 zeolite as the shell

A highly selective Raney Fe@H-ZSM-5 core shell catalyst was synthesized by Sun et al. and showed excellent selectivity to C<sub>5</sub>–C<sub>11</sub> hydrocarbons (71%) and unexpectedly enhanced C<sub>5+</sub> selectivity [122]. By comparison, when Raney Fe alone and the physical mixture of Raney Fe and H-ZSM-5 were tested, worse catalytic performances with C<sub>5</sub>–C<sub>11</sub> selectivity lower than 50% were found. The outstanding selectivity of the core shell catalyst to C<sub>5</sub>–C<sub>11</sub> hydrocarbons was attributed to the higher concentration of Hagg carbide ( $\chi$ -Fe<sub>5</sub>C<sub>2</sub>) which was stabilized because of the hydrophilic H-ZSM-5 shell. This hydrophilic shell facilitated the enrichment of the more oxidizing H<sub>2</sub>O byproduct than the syngas and hydrocarbons thereby decreasing the oxidative environment of the oxidation-susceptible Hagg carbide in the Raney Fe core part. This design of using the H-ZSM-5 shell to modify the chemical state of the Raney Fe core to improve the catalytic performance is encouraging to open up more avenues in this area for zeolite based core shell catalyst.

Co/SiO<sub>2</sub>@H-ZSM-5 bifunctional core shell catalyst was prepared via hydrothermal method by Sartipi et al. to directly produce C<sub>3</sub>–C<sub>7</sub> hydrocarbons from syngas [123]. Compared with uncoated Co/SiO<sub>2</sub> after hydrothermal aging catalyst and physical mixture of Co/SiO<sub>2</sub> and H-ZSM-5 catalyst (Fig. 11), core shell Co/SiO<sub>2</sub>@H-ZSM-5 catalyst showed similar C<sub>1</sub> selectivity, higher C<sub>3</sub>–C<sub>7</sub> selectivity and lower selectivity for C<sub>8+</sub> especially for C<sub>12+</sub> hydrocarbons. The authors attributed the outstanding selectivity of core shell catalyst to the close vicinity of the active Co/SiO<sub>2</sub> and the acidity of the shell. In addition, even though Co/SiO<sub>2</sub>@Silicalite-1 formed core shell structure, it deactivated almost in the initial stage due to the accumulation of long chain hydrocarbons at Co/SiO<sub>2</sub> active phase as a result of the absence of acidity of Silicalite-1 shell. This illustrated the importance of acidity of the core shell structure. However, the authors found that the activity of the core shell Co/SiO<sub>2</sub>@H-ZSM-5 catalyst decreased in terms of CO conversion compared with Co/SiO<sub>2</sub> because of the decreased diffusion rate of long chain hydrocarbons through the H-ZSM-5 shell. Instead of modifying the porosity of H-ZSM-5 shell, the authors developed another bifunctional catalyst, Co deposited on mesoporous H-ZSM-5, to realize the close vicinity of Co and the acidity of H-ZSM-5, the high accessibility of Co active species and high mass transfer efficiency of the products. This supported catalyst showed both high activity and selectivity. However, the improvement of activity of the core shell Co/SiO<sub>2</sub>@H-ZSM-5 catalyst also can be achieved by tuning the porosity or making the H-ZSM-5 shell thinner to increase the diffusion rate of long chain hydrocarbons.

Yang et al. synthesized two kinds of core shell catalysts: Co/SiO<sub>2</sub>@Silicalite-1@H-ZSM-5 and Co/SiO<sub>2</sub>@H-ZSM-5 by improved hydrothermal synthesis method and physically adhesive method respectively for one pot production of light isoparaffin by F-T synthesis [124]. These two core shell catalysts showed excellent catalytic selectivity with isoparaffin selectivity of 49.3% and 43.8% and C<sub>11+</sub> selectivity of 0.4% and 1.2% respectively. By comparison, worse catalytic selectivity for Co/SiO<sub>2</sub> alone and physical mixture of Co/SiO<sub>2</sub> and H-ZSM-5 were obtained. The better catalytic selectivity of the core shell catalysts were attributed to the confined reaction space and the synergistic effect between the Co/SiO<sub>2</sub> core and H-ZSM-5 shell. Co/SiO<sub>2</sub> core and H-ZSM-5 shell acted as the conventional F-T synthesis catalyst to produce long chain hydrocarbons and the secondary isomerization/hydrocracking catalyst to produce light isoparaffin respectively. These two reactions conducted orderly and cooperatively, making the core shell catalysts excellent to realize direct production of light isoparaffin from syngas (Fig. 12). However, it is noted that the selectivity of normal paraffin for these two core shell catalysts are still quite high (49.7% and 47.6%, respectively). These two values are close to that of the physical mixture of Co/SiO<sub>2</sub> and H-ZSM-5. This indicates that

the shell parameters of H-ZSM-5 such as thickness should also be optimized to enhance the efficiency of hydrocracking reactions to produce isoparaffin.

### 3.1.2. Other zeolites as the shell

Cr/ZnO core SAPO-46 zeolite shell catalyst was developed by Pinkaew et al. to directly produce dimethyl ether (DME) via one step F-T synthesis with methanol as intermediate product [125]. The core shell catalyst combined together the two active sites: Cr/ZnO core for methanol synthesis and SAPO-46 zeolite shell for dehydration of methanol to produce DME. The selection of SAPO-46 zeolite was based on its effectiveness to suppress further dehydration of DME to other alkene/alkane. Compared with Cr/ZnO alone and the physical mixture of Cr/ZnO and SAPO-46 zeolite, the core shell catalyst showed a comparable CO conversion but obviously higher DME selectivity. The advantages of the core shell structure are: providing more opportunities for methanol to diffuse through the SAPO-46 shell and maximizing the contact area between Cr/ZnO and the shell without minimizing the diffusion rate of both reactants and products. These advantages can shift the reaction equilibrium toward DME caused by the efficient consumption and diffusion of the intermediate methanol, leading to higher CO conversion and higher DME selectivity. Even though the authors claimed that their method used to coat the SAPO-46 shell on Cr/ZnO core can avoid the destruction of the core shell structure, the structural integrity should be reconfirmed after reaction.

Lin et al. synthesized another bifunctional core shell catalyst with fused iron (FI) as the core and H-Mordenite (MOR) zeolite as the shell for the production of isoparaffin via one step F-T synthesis (Fig. 13) [126]. The FI core acted as the F-T catalyst to convert syngas to heavy waxy hydrocarbons; while the MOR shell played the role of hydrocracking and isomerizing the waxy hydrocarbons. By forming core shell structure, the intimate contact between the core and the shell could efficiently decompose the heavy hydrocarbons deposited on the FI surface, accelerating the reactants diffusion and adsorption. In addition, collision possibility between linear hydrocarbons and acidic sites in zeolite was enhanced, resulting in higher selectivity to middle isoparaffins. Furthermore, the core shell structure catalyst was extremely selective to produce isoparaffins compared with FI alone and physical mixture of FI and MOR. This property can be attributed to the two effects of the core shell structure: (1) allowing the free diffusion of linear normal paraffins to be isomerized to short isoparaffins; (2) restricting the escaped branched isoparaffins to diffuse back to the core. The design strategy used in this study was interesting and the core shell catalyst showed excellent selectivity to isoparaffins. Whereas, it would be much better if long term stability test for this catalyst could be provided to show its promising industrial application.

## 3.2. Selective hydrogenation of acetylenic compounds

Selective hydrogenation of C–C triple bonds (C≡C) to C–C double bonds (C=C) is very important because this reaction is involved in the production of a wide range of intermediates for fine chemicals and daily necessities [127]. However, C≡C are easily to be fully hydrogenated to C–C single bonds by the active metal catalysts such as Pd and Pt with low selectivity to C=C [128,129]. There are mainly two effects which can be accounted for the increase of hydrogenation selectivity: (1) changing of the electronic density of active metal (for example, by forming bimetallic alloy or reacting with an organometallic precursor) which may affect the relative adsorption strength of the reactant, intermediates and hydrogen; (2) altering of the geometry of the active site as a result of the blockage of active metal surface by another metal (for example, Pb [130], Ag [131] and Zn [132]). As for core shell catalysts design for alkynes hydrogenation, their high selectivity can be mainly attributed to the



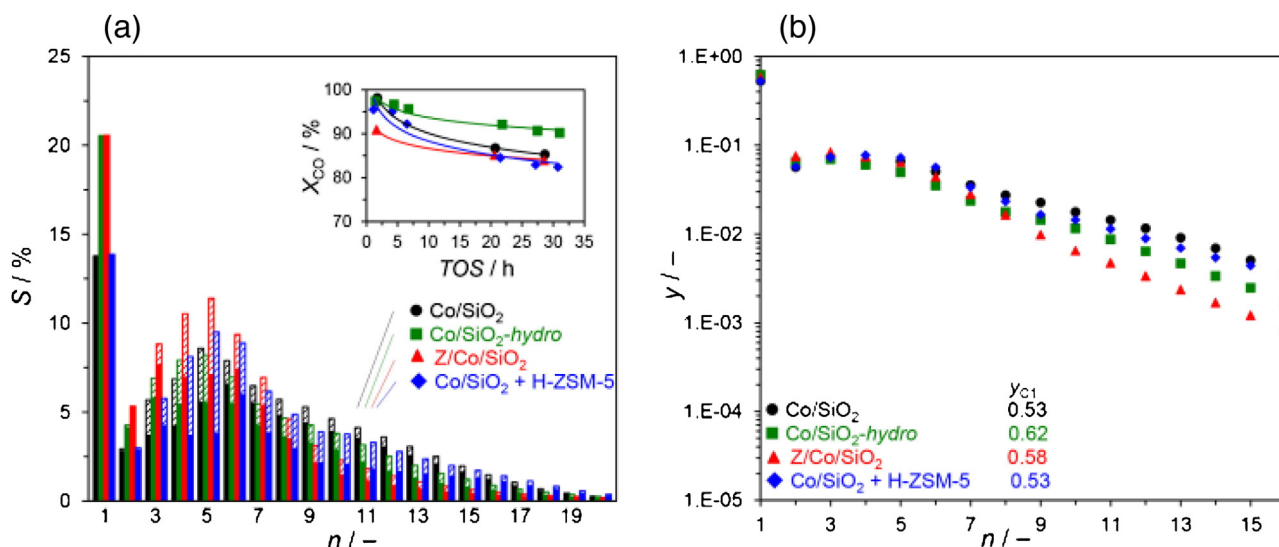


**Fig. 11.** a) Carbon selectivity and b) Molar distribution of FTS products after 20 h on-stream at 533 K, 10 bar,  $H_2/CO = 2$  and  $GHSV = 25.8 \text{ m}^3_{STP} \text{ kg}^{-1} \text{ Co h}^{-1}$ ; ■:  $n$ -paraffins; ///: sum of isoparaffins and olefins;  $y_{C1}$ : methane molar fraction. Insert in (a) shows the time-on-stream (TOS) evolution of CO conversion. Reprinted with permission from Ref. [123], copyright (2013) Elsevier.

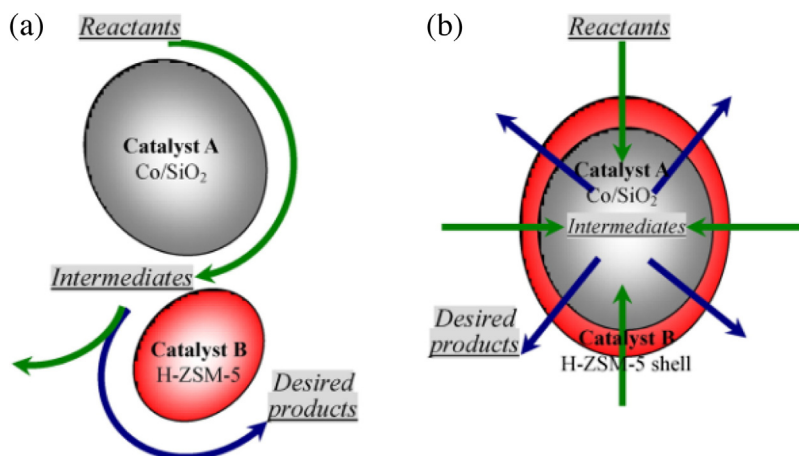


**Fig. 12.** The schematic representation of tandem catalysis process happened on the multifunctional catalyst with different assembly structure: (a) physically mixed catalyst. (b) core-shell-like capsule catalyst. Reprinted with permission from Ref. [124], copyright (2013) Elsevier.

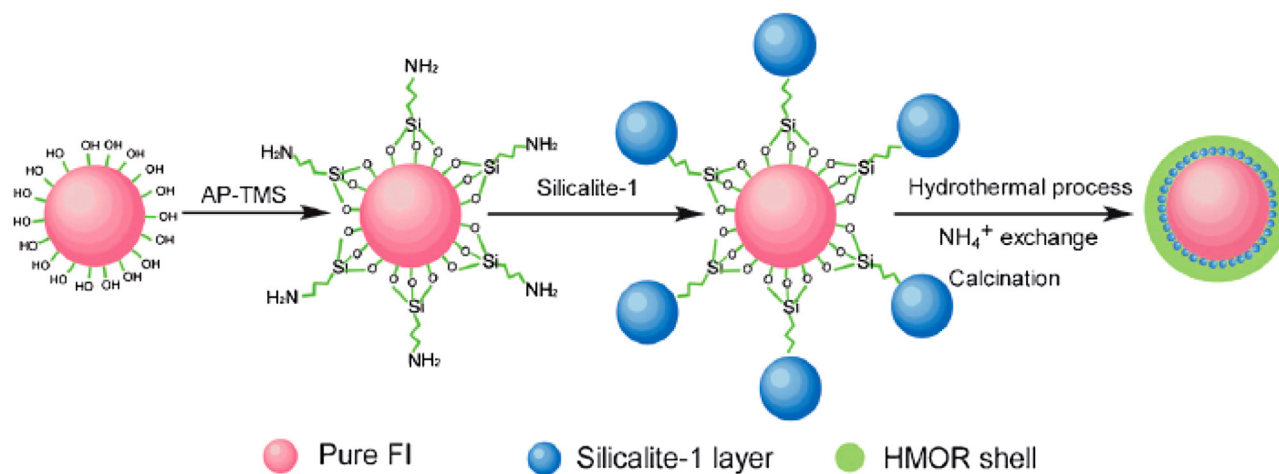


**Fig. 13.** Schematic image about the synthesis procedure of HMOR/FI capsule catalyst without template. Reprinted with permission from Ref. [126], copyright (2013) John Wiley and Sons.

blockage of active sites which are active for the secondary hydrogenation reactions by the shell. In the following, design strategies of highly selective core/yolk shell catalysts for C=C hydrogenation will be introduced.

Pd nanoparticles (PdNPs) encapsulated by methyl-3-trimethoxysilylpropylsulfonate (MPSO) supported on SiO<sub>2</sub> surface, for semi-hydrogenation of alkynes was designed by Mitsudome and coworkers (Fig. 14) [133]. By forming MPSO shell, selective access of alkynes to the Pd active sites due to their stronger coordination ability than that of alkenes and MPSO prevented the over-hydrogenation and isomerization of alkenes, leading to higher alkenes selectivity. The Pd@MPSO/SiO<sub>2</sub>-1 core shell catalyst exhibited higher stereo-selectivity and excellent yield to 1-phenyl-1-propene in the hydrogenation of 1-phenyl-1-propyne reaction compared with Pd supported on SiO<sub>2</sub> catalyst, Pd supported on surface modified SiO<sub>2</sub> with MPSO catalyst and the commercial catalysts (Pd/C, Pd/Al<sub>2</sub>O<sub>3</sub>, and Pd/TiO<sub>2</sub>). In addition, Pd@MPSO/SiO<sub>2</sub>-1 can convert various aromatic and aliphatic internal alkynes into the corresponding alkenes with high yields without the occurrence of over-hydrogenation and isomerization. While the Pd@MPSO/SiO<sub>2</sub>-2 core shell catalyst showed excellent selectivity to styrene with conversion >99% for the semi-hydrogenation of ethynylbenzene terminal alkyne. Similarly, Pd@MPSO/SiO<sub>2</sub>-2 catalyst also can be extended to semi-hydrogenate a wide range of terminal alkynes with excellent selectivity and compatibility of other reducible functional groups such as halogen, aldehyde and nitro moieties. The idea that combining materials with different coordination ability to the reactants and products formed in the core-shell structure to achieve excellent selectivity provides a new design method.

Erokhin et al. synthesized Fe@C and Ni@C core-shell nanoparticles for semi-hydrogenation of phenylacetylene (PA) reaction [134]. The authors found that only defects-rich areas of the carbon shells of these two core shell catalysts were feasible to activate H<sub>2</sub> by dissociative adsorption which is the key step for hydrogenation reactions. This was attributed to the fact that the chemisorption energies can be significantly decreased only for the imperfect areas of graphene with the presence of the transition metal core. For Ni@C, the defected graphene areas for styrene (ST) formation were active at low temperatures. Therefore selectivity for ST decreased with the increase of temperature due to the involvement of non-defective and non-selective graphene areas in catalytic action. By comparison, for Fe@C, more selective defected graphene areas become active at higher reaction temperatures. Consequently, selectivity for ST formation increased with the increase of temperature. The excellent catalytic performance: 86% ST selectivity and 99% PA conversion was obtained at 300 °C. This study revealed that the active sites for semi-hydrogenation of phenylacetylene were located within the carbon shell instead of the metal core nor at the interface between the carbon shell and metal core. The study method-combining the experiments and DFT calculation-was persuasive in providing adequate data which correlates both theoretical assumption and practical results.

Liang's group synthesized cubic Pd@ZIF-8 metal organic frameworks core shell nanocatalyst for hydrogenation of 1,4-butanediol (BYD) with excellent selectivity to 1,4-butanediol (*cis*-BED) (Fig. 15) [135]. This high *cis*-BED selectivity was achieved by blocking the edge and vertex sites of Pd which are active for the secondary hydrogenation reaction of *cis*-BED to 1,4-butanediol (BDO) by ZIF-8 directed by the preferential adsorption of PVP on these sites. In addition, the narrow pore channels and the N containing ligand (2-methylimidazole) of ZIF-8 may also contribute to this high selectivity by limiting the isomerization reactions and adjusting the selectivity respectively. Pd@ZIF-8 with 1 wt% Pd loading exhibited 99.7% conversion of BYD with 97.5% selectivity to *cis*-BED at 50 °C. Further increasing Pd loading and reaction temperature decreased

*cis*-BED selectivity due to the un-encapsulated Pd on the edge of ZIF-8 and the promotion of deep hydrogenation reaction, respectively. The core shell catalyst showed excellent selectivity and stability even after five runs (Fig. 15c). However, it is noted that the Pd loading of Pd@ZIF-8 core shell catalyst was limited below 5 wt%. Therefore, an improvement in the synthesis method to encapsulate more amounts of nanoparticles by ZIF-8 is necessary for these core shell materials to be widely used in other catalytic applications.

### 3.3. Other shape and size selectivity design

#### 3.3.1. Shape selectivity

Ag@CeO<sub>2</sub> core shell catalyst and Ag@CeO<sub>2</sub> core shell supported on CeO<sub>2</sub> nanocomposite (Ag@CeO<sub>2</sub>/CeO<sub>2</sub>) were synthesized by Mitsudome et al. for selective reduction of unsaturated aldehydes [136]. Compared with Ag/CeO<sub>2</sub> supported catalysts, Ag alone and CeO<sub>2</sub> alone, Ag@CeO<sub>2</sub> core shell catalyst exhibited superiorly high chemoselectivity to reduce citral to allylic alcohols geraniol and nerol. More or less Ce will result in either hindering of reactants to Ag or leaving Ag non-encapsulated, leading to decrease of activity or selectivity. When Ag@CeO<sub>2</sub> was deposited on CeO<sub>2</sub> support, much higher activity was found while maintaining the selectivity to allylic alcohols. Ag@CeO<sub>2</sub>/CeO<sub>2</sub> also efficiently converted a wide range of aldehydes to the corresponding allylic alcohols with high selectivity. By forming core shell structure, interaction between Ag and the basic sites of CeO<sub>2</sub> was maximized, leading to the heterolytic cleavage of H<sub>2</sub> to the Ag-hydride and proton active species. These species preferred polar functional groups over C=C bonds, resulting in the outstanding shape selectivity of the core shell catalyst. By depositing the core shell structure on CeO<sub>2</sub>, sintering was prevented, resulting in higher activity and durability. This study revealed a good design method to improve catalyst activity while retaining the selectivity. Nevertheless, it could be better if characterizations for the spent catalysts can be done to verify the structural stability.

Another type of shape selective catalyst, Mo supported on H-ZSM-5 core@Silicalite-1 shell, was designed by Jin et al. for CH<sub>4</sub> dehydroaromatization (MDA) reaction [137]. The high aromatic selectivity for the core shell catalyst was achieved by: covering some Brønsted acid sites on the external surface of H-ZSM-5 core by Silicalite-1 shell to release the formation of carbonaceous deposits; preventing the migration of Mo species into the pores of H-ZSM-5 by Silicalite-1 shell weakening the synergy effect between the acid sites on H-ZSM-5 and Mo species. Stable and high benzene selectivity of 60% for the core shell catalyst was obtained compared with the 45% for Mo supported on H-ZSM-5 catalyst. The selectivity to toluene and xylene exhibited the same trend with benzene. However, the selectivity for nonaromatics was significantly suppressed due to the decrease of the number of external Brønsted acid sites. Thicker Silicalite-1 shell did not bring about higher selectivity but higher stability. This design method to improve selectivity through core shell structure is promising to be widely applied.

Gawande et al. designed the bimetallic Ag@Ni core shell magnetic nanocatalyst for transfer hydrogenation reactions of aromatic nitro and carbonyl compounds [138]. The excellent chemoselectivity and regioselectivity of the core shell catalyst was independent on the nature and position of the substituents on the aromatic nitro compounds. A series of halogenated nitrobenzenes were selectively hydrogenated to the corresponding halogenated amines without any dehalogenation. In addition, carbonyl compounds can be converted to the corresponding alcohols with excellent yields above 90%. Similarly, no dehalogenation of the halogen derivatives of acetophenones was observed. The mechanism for the reduction of aromatic nitro compounds was proposed: hydride transfer between the adsorbed isopropanol and intermediate nitro compounds on Ag@Ni surface occurred followed by water elimination

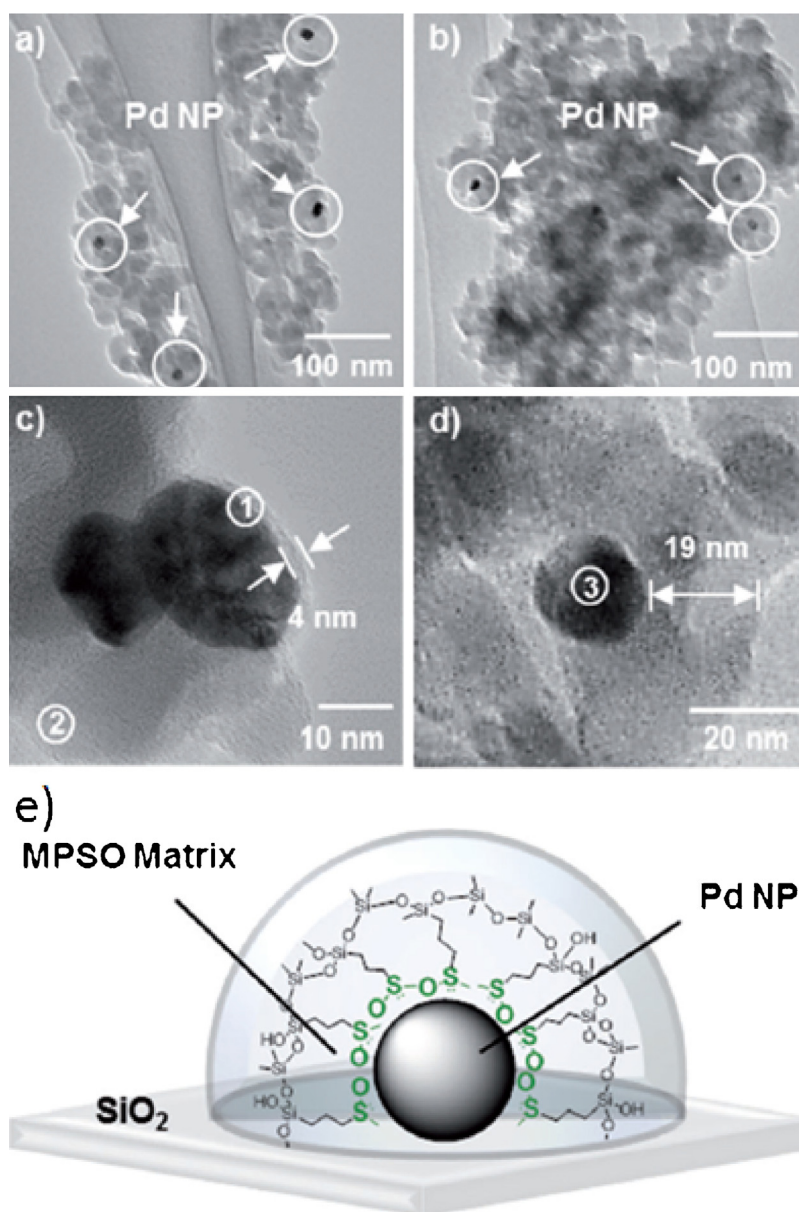


**Fig. 14.** TEM images of (a), (c) Pd@MPSO/SiO<sub>2</sub>-1 and (b), (d) Pd@MPSO/SiO<sub>2</sub>-2; (e) schematic illustration of the core-shell structured Pd@MPSO/SiO<sub>2</sub>. Reprinted with permission from Ref. [133], copyright (2013) John Wiley and Sons.

to obtain the reduced product. The excellent shape selectivity of Ag@Ni was impressive.

### 3.3.2. Size selectivity

As described earlier, catalyst size selectivity in terms of core shell nanostructures usually was achieved by tuning the pore size of the porous shell. Recently, the size selectivity of core shell nanostructures with metal organic frameworks (MOFs) as the shell such as ZIF-8, HKUST-1, UiO-66, NH<sub>3</sub>-UiO-66 and NH<sub>3</sub>-MIL-53 encapsulating nanoparticles as the core have been widely studied due to the easily tuned nanopores, shape and chemical properties of MOFs and their molecular sieving capability. Therefore, in the following, these size selective nanoparticles core@MOF shell nanostructures and other size selectivity design examples will be introduced.

A series of core shell size selective catalysts with various MOF materials such as UiO-66, NH<sub>3</sub>-UiO-66 and NH<sub>3</sub>-MIL-53 as the shell were developed by Huo's group [139]. Hydrogenation of olefins with different molecular size using Pt@UiO-66 shell was performed.

It was found that the conversion rates decreased with the increase of the olefins molecular size. 100% conversion after 24 h reaction was found for 1-hexene compared with 65.99% for cyclooctene, 35% for *trans*-stilbene, 8% for triphenyl ethylene and 0% for tetraphenyl ethylene. These results were attributed to the different diffusion barrier caused by the pore aperture of the UiO-66 frame. This study enriches the core shell nano-structures as novel materials for a wide range of application.

Kuo et al. synthesized another size selective yolk shell Pd@ZIF-8 MOF catalyst using CuO as the sacrificial template for gas phase hydrogenations of ethylene, cyclohexene and cyclooctene (Fig. 16) [82]. Small ethylene molecules can diffuse to the Pd active sites through the pores of ZIF-8. Therefore, all the three different structural catalysts: Pd@ZIF-8 core shell, Pd@ZIF-8 yolk shell and Pd supported on ZIF-8 showed the same high activity for ethylene conversion. By comparison, no detectable activity of cyclooctene was found for both the core shell and yolk shell structure catalysts due to its bigger molecular size than the pore size of ZIF-8, leading to



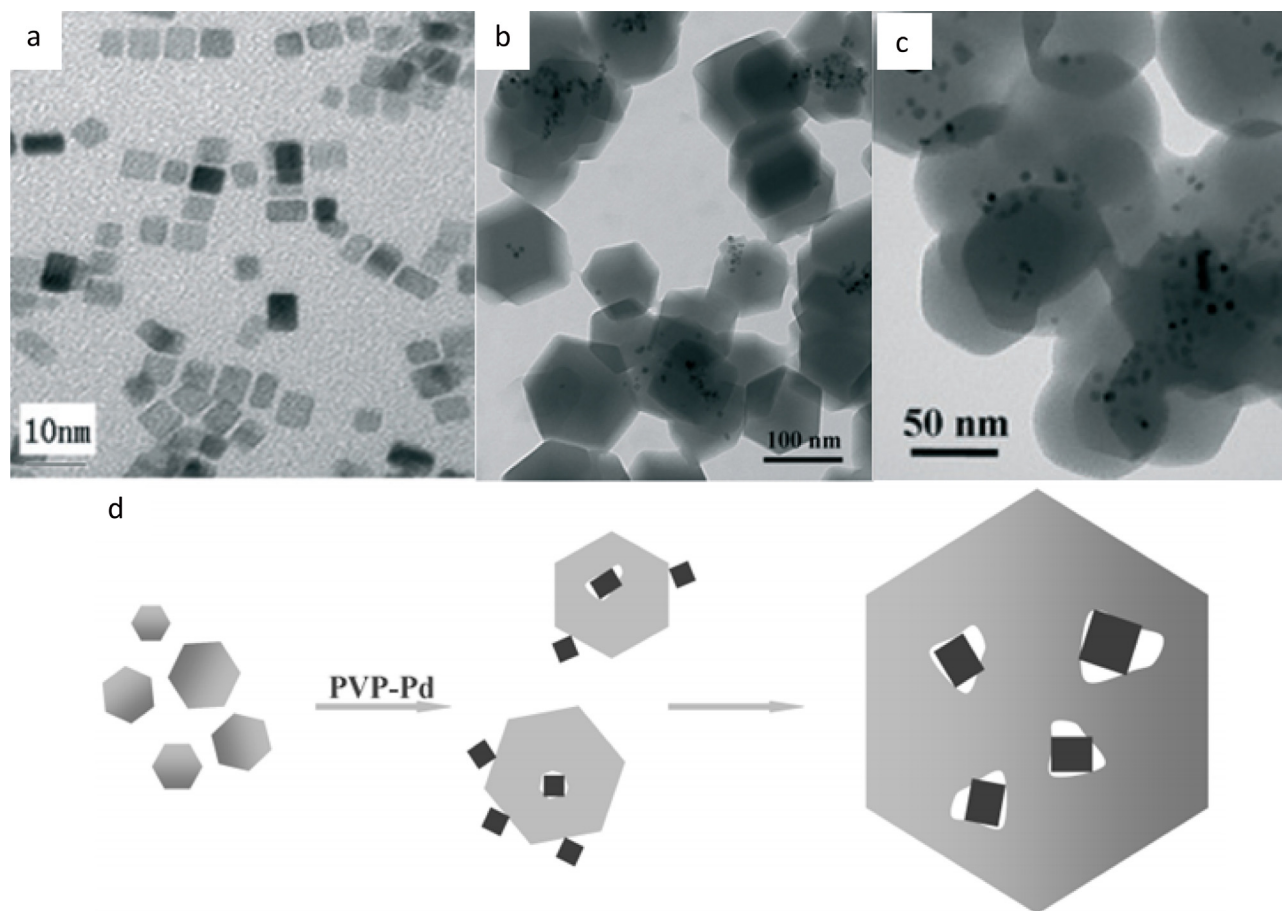


**Fig. 15.** TEM images of PVP-Pd colloid (a), 1 wt% PVP-Pd@ZIF-8: fresh catalyst (b) and used catalyst (c); (d) schematic illustration of preparation of PVP-Pd@ZIF-8 catalysts. Reprinted with permission from Ref. [135], copyright (2014) Royal Society of Chemistry.

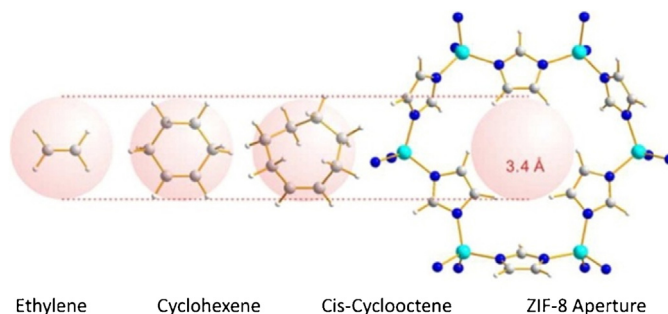


**Fig. 16.** Schematic illustration of molecular-size-selective catalysis. Reprinted with permission from Ref. [82], copyright (2012) American Chemical Society.

difficult access to the active Pd sites. While for cyclohexene, the yolk shell structure and Pd/ZIF-8 supported catalyst showed similar but higher activation energy compared to that of the core shell structure catalyst. One of the possible explanations is based on the diffusion limitation caused by the comparable sizes of cyclohexene and the pore aperture of ZIF-8. Different diffusion regime between core shell and yolk shell structure catalysts could also result in the different catalytic activity. The synthetic method in this study is promising for design of other size selective yolk shell structure MOF catalysts.

#### 3.4. Other design examples for high selectivity

Zhao's group designed the ultrastable Y zeolite core@Al doped mesosilica shell (USY@Al- mesosilica) catalyst for cracking Iran

VGO-2 heavy oil and the *n*-hexadecane probe molecule [140]. The core shell catalyst combines the weak acid sites on the mesoporous silica shell introduced by Al doping and the strong acid sites of USY core with micropores. The weak acid sites on the shell preliminary cracked heavy molecules to slightly smaller molecules which can diffuse easier to the strong acid sites on the core part for further cracking. In addition, the cracking products can diffuse out fast through the *meso*-porous shell to avoid further cracking. The USY@Al- mesosilica core shell catalyst can effectively improve the C<sub>5</sub>–C<sub>15</sub> liquid yield for cracking of *n*-hexadecane compared to USY alone, Al-SBA-15 alone and the physical mixture of USY and Al-SBA-15. As for hydrocracking of VGO-2 heavy oil, NiW supported on USY@Al- mesosilica core shell catalyst with 60 nm shell thickness showed high yield and selectivity for the middle distillates. The delicate design of combining the advantages of both the core and

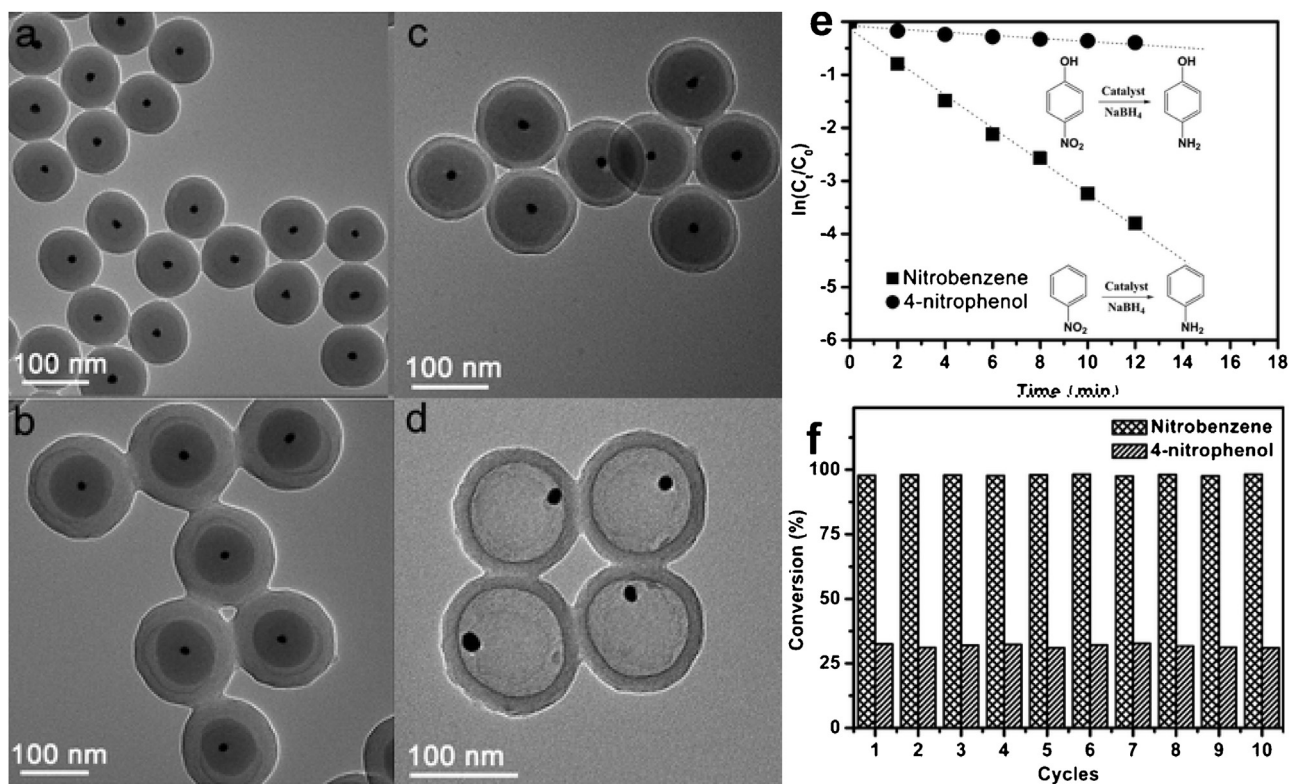


**Fig. 17.** TEM images of (a) Au@SiO<sub>2</sub> core-shell nanoparticles, (b) Au@SiO<sub>2</sub>@RF trilayer composites, (c) Au@SiO<sub>2</sub>@C composites, and (d) Au@C yolk-shell particles after the removal of silica. (e) Kinetic analysis of the catalytic reductions for nitrobenzene and 4-nitrophenol. (f) Conversions of nitrobenzene and 4-nitrophenol in 10 successive cycles of reduction with yolk-shell Au@C. Reprinted with permission from Ref [141], copyright (2013) Royal Society of Chemistry.

shell material showed a good example to prepare multifunctional catalysts by forming core shell structure.

Guan et al. synthesized various nanostructures including core-shell, hollow and yolk-shell structures with hydrophobic carbon and resorcinol-formaldehyde resin polymer respectively as the shell via a versatile cooperative template-directed coating method (Fig. 17) [141]. Among them, Au@hydrophobic microporous carbon yolk-shell catalyst showed higher selectivity and one order of magnitude higher apparent rate constant to reduce hydrophobic nitrobenzene than the hydrophilic 4-nitrophenol. This suggested that the hydrophobic carbon shell favored the diffusion of hydrophobic reactants to the active core. By comparison, the nitric acid treated Au@carbon yolk shell catalyst which had more hydrophilic carbon shells exhibited higher rate constant for 4-nitrophenol than that of nitrobenzene, illustrating the more favorable diffusion of hydrophilic reactants for this catalyst. Au@carbon yolk shell catalyst maintained the 98% conversion for nitrobenzene even after 10 successive cycles of reactions (Fig. 17f), suggesting its structural stability. The idea to design selective catalyst through controlling the surface hydrophobicity of the shell is certainly interesting and should be explored.

#### 4. Conclusions and outlook

Developing catalysts with high activity, extreme stability and excellent selectivity is the goal for all catalysis researchers. Nano catalysts are wellknown for their high activity but they suffer from instability problems. The significant progress in nanotechnology such as nanomaterial synthesis [142], characterization equipment and surface science techniques as well as molecular simulation paves the way for improving the stability of nanocatalysts through rational design. Among the proposed design measures, forming

core/yolk shell structure turns out to be the most efficient and interesting method which has been intensively investigated.

In this review, design strategies for core/yolk shell nanocatalysts to achieve high stability and selectivity are summarized and exemplified with the progress made in the recent three years. The principles of the core shell catalysts to achieve high stability and selectivity are listed as below. To achieve high stability, active sites of the catalysts should be embedded in the core or within the porosity controllable shell. In this way, sintering of these active sites can be prevented while keeping their accessibility when they are employed in the high temperature energy related fields such as hydrocarbon reforming for syngas production, high temperature fuel cells such as SOFC, MCFC and CO oxidation reaction. In addition, other properties for specific applications, for instance, carbon deposition resistance for syngas production and corrosion resistance for MCFC also can be attained.

To achieve high selectivity, the catalytic active sites for the unwanted side reactions can be poisoned or covered by forming the core shell structure. In addition, high selectivity also can be attained by regulating the diffusion rate of both reactants and products to the active sites through tuning the shell porosity, pore size, shell hydrophobicity and shell thickness; adjusting and maintaining the active metal particle size with shell protection and maximizing the synergy effect between the active metal and shell material. For example, by combining the two active sites for F-T synthesis and the secondary hydrocracking reactions together to form bifunctional core/yolk shell structure, high selectivity to a certain range of carbon length can be obtained for F-T synthesis.

Even though great achievements have been made in core/yolk shell structure design, several issues need to be improved before these catalysts can be industrially produced and applied. Firstly, the tedious multistep synthesis methods with only tiny yield of nanocatalysts should be replaced with the more facile method

which can simultaneously be applied for large scale production. In developing new synthesis procedures, factors such as industrial scalability and environmental feasibility should be considered. Secondly, it is observed that most of the studies of core/yolk shell structures are focused on material synthesis prior to catalytic application testing. However, detailed explanations to their outstanding catalytic performances are, to some extent, insufficient and lack of experimental evidences. This could be progressively improved with the rapid advancement of both experimental and characterization techniques. Thirdly, it is well known that the reaction condition should be determined by excluding the diffusion limitation problem before performing catalytic tests among different catalysts. This is especially true and should not be omitted for the core shell catalysts since reactants and products reach and leave the active sites of the catalysts by diffusion in and out of the porous shell. Therefore, methods should be carefully taken to exclude the diffusion limitation as stated by H. Ribeiro [143]. Finally, most of the core/yolk shell nanocatalyst designs are based on the catalytic mechanisms from the corresponding supported catalysts or driven by the intrinsic structural advantages of the core/yolk shell structure such as high temperature sintering resistance and leaching prevention of active metal. Some core/yolk shell nanocatalysts are even synthesized first and ultimately found their amazing catalytic application for a certain reaction after several times trying. This trial and error design method should be improved by understanding the mechanism which occurs during the catalytic processes and the dynamic behavior of the active sites of core/yolk shell nanocatalysts with the help of *in situ* surface-science techniques and computer calculations such as density functional theory (DFT) simulations. Understanding these underlining mechanisms of core/yolk shell nanocatalysts in a molecule level is of paramount importance especially in designing more sophisticated nanostructures with multifunctionalities. In addition, combining the reaction kinetics with the mechanism can lead to design of core/yolk shell nanocatalyst for more upstream industrial applications.

## Acknowledgements

The authors gratefully thank the National University of Singapore (FRC project WBS R-279-000-407-112), the China Scholarship Council and NRF (NRF-POC 001-055) for generously supporting this work.

## Appendix A. Supplementary data

Supplementary data associated with this article can be found, in the online version, at <http://dx.doi.org/10.1016/j.apcatb.2016.01.067>.

## References

- [1] M.A. Mahmoud, R. Narayanan, M.A. El-Sayed, *Acc. Chem. Res.* 46 (2013) 1795–1805.
- [2] B.C. Gates, *Chem. Commun.* 49 (2013) 7876–7877.
- [3] T.W. Hansen, A.T. DeLaRiva, S.R. Challa, A.K. Datye, *Acc. Chem. Res.* 46 (2013) 1720–1730.
- [4] G. Melaet, A. Lindeman, G. Somorjai, *Top. Catal.* 57 (2014) 500–507.
- [5] A. Cao, R. Lu, G. Vesper, *Phys. Chem. Chem. Phys.* 12 (2010) 13499–13510.
- [6] L. de Rogatis, M. Cargnello, V. Gombac, B. Lorenzutti, T. Montini, P. Fornasiero, *ChemSusChem* 3 (2010) 24–42.
- [7] A. Ungureanu, B. Dragoi, A. Chiriac, C. Ciotonea, S. Royer, D. Duprez, A.S. Mamede, E. Dumitriu, *ACS Appl. Mater. Inter.* 5 (2013) 3010–3025.
- [8] L. Yang, M. Qi, M. Jin, *CrystEngComm* 15 (2013) 2804–2808.
- [9] C. Wu, L. Dong, J. Onwudili, P.T. Williams, J. Huang, *ACS Sustain. Chem. Eng.* 1 (2013) 1083–1091.
- [10] K.A. Dahlberg, J.W. Schwank, *Chem. Mater.* 24 (2012) 2635–2644.
- [11] X. Zhang, Y.C. Guo, Z. Cheng Zhang, J.S. Gao, C.M. Xu, *J. Catal.* 292 (2012) 213–226.
- [12] D. Deng, L. Yu, X. Chen, G. Wang, L. Jin, X. Pan, J. Deng, G. Sun, X. Bao, *Angew. Chem. Int. Ed.* 52 (2013) 371–375.
- [13] C. Galeano, J.C. Meier, V. Peinecke, H. Bongard, I. Katsounaros, A.A. Topalov, A. Lu, K.J.J. Mayrhofer, F. Schüth, *J. Am. Chem. Soc.* 134 (2012) 20457–20465.
- [14] Q.-L. Zhu, J. Li, Q. Xu, *J. Am. Chem. Soc.* 135 (2013) 10210–10213.
- [15] K. Sutthiumporn, T. Maneerung, Y. Kathiraser, S. Kawi, *S. Int. J. Hydrogen Energy* 37 (2012) 11195–11207.
- [16] U. Oemar, M.L. Ang, W.F. Hee, K. Hidajat, S. Kawi, *Appl. Catal. B: Environ.* 148 (2014) 231–242.
- [17] Y. Kathiraser, W. Thitsartarn, K. Sutthiumporn, S. Kawi, *J. Phys. Chem. C* 117 (2013) 8120–8130.
- [18] D.V. Cesar, M.A.S. Baldanza, C.A. Henriques, F. Pompeo, G. Santori, J. Múnera, E. Lombardo, M. Schmal, L. Cornaglia, N. Nichio, *Int. J. Hydrogen Energy* 38 (2013) 5616–5626.
- [19] X. Du, D. Zhang, L. Shi, R. Gao, J. Zhang, *Nanoscale* 5 (2013) 2659–2663.
- [20] M. Koike, D. Li, Y. Nakagawa, K. Tomishige, *ChemSusChem* 5 (2012) 2312–2314.
- [21] E.T. Saw, U. Oemar, X.R. Tan, Y. Du, A. Borgna, K. Hidajat, S. Kawi, *J. Catal.* 314 (2014) 32–46.
- [22] D. Li, Y. Nakagawa, K. Tomishige, *Appl. Catal. A: Gen.* 408 (2011) 1–24.
- [23] Z. Li, L. Mo, Y. Kathiraser, S. Kawi, *ACS Catal.* 4 (2014) 1526–1536.
- [24] Z. Li, Y. Kathiraser, J. Ashok, U. Oemar, S. Kawi, *Langmuir* 30 (2014) 14694–14705.
- [25] L. Mo, S. Kawi, *J. Mater. Chem. A* 2 (2014) 7837–7844.
- [26] Z. Li, Y. Kathiraser, S. Kawi, *ChemCatChem* 7 (2014) 160–168.
- [27] I. Lee, M.A. Albitzer, Q. Zhang, J. Ge, Y. Yin, F. Zaera, *Phys. Chem. Chem. Phys.* 13 (2011) 2449–2456.
- [28] S.H. Joo, J.Y. Park, C.-K. Tsung, Y. Yamada, P. Yang, G.A. Somorjai, *Nat. Mater.* 8 (2009) 126–131.
- [29] P.M. Arnal, M. Comotti, F. Schüth, *Angew. Chem. Int. Ed.* 45 (2006) 8224–8227.
- [30] L. Liu, Y. Qi, J. Lu, S. Lin, W. An, Y. Liang, W. Cui, *Appl. Catal. B: Environ.* 183 (2016) 133–141.
- [31] M.A. Lucchini, A. Testino, A. Kambolis, C. Proff, C. Ludwig, *Appl. Catal. B: Environ.* 182 (2016) 94–101.
- [32] Y.-W. Lee, J.-Y. Lee, D.-H. Kwak, E.-T. Hwang, J.I. Sohn, K.-W. Park, *Appl. Catal. B: Environ.* 179 (2015) 178–184.
- [33] S. Ullah, E.P. Ferreira-Neto, A.A. Pasa, C.C.J. Alcántara, J.J.S. Acuña, S.A. Bilmes, M.L. Martínez Ricci, R. Landers, T.Z. Fermino, U.P. Rodrigues-Filho, *Appl. Catal. B: Environ.* 179 (2015) 333–343.
- [34] Y. Wei, J. Jiao, Z. Zhao, J. Liu, J. Li, G. Jiang, Y. Wang, A. Duan, *Appl. Catal. B: Environ.* 179 (2015) 422–432.
- [35] Y. Zhang, Y. Zhou, Z. Zhang, S. Xiang, X. Sheng, S. Zhou, F. Wang, *Dalton Trans.* 43 (2014) 1360–1367.
- [36] J. Zhou, B. Duan, Z. Fang, J. Song, C. Wang, P.B. Messersmith, H. Duan, *Adv. Mater.* 26 (2014) 701–705.
- [37] X. Fang, J. Zang, X. Wang, M.-S. Zheng, N. Zheng, *J. Mater. Chem. A* 2 (2014) 6191–6197.
- [38] M.B. Gawande, A. Goswami, T. Asefa, H. Guo, A.V. Biradar, D.-L. Peng, R. Zboril, R.S. Varma, *Chem. Soc. Rev.* 44 (2015) 7540–7590.
- [39] S.W. Kang, Y.W. Lee, Y. Park, B.-S. Choi, J.W. Hong, K.-H. Park, S.W. Han, *ACS Nano* 7 (2013) 7945–7955.
- [40] J. Chen, R. Zhang, L. Han, B. Tu, D. Zhao, *Nano Res.* 6 (2013) 871–879.
- [41] Q. Zhang, I. Lee, J. Ge, F. Zaera, Y. Yin, *Adv. Funct. Mater.* 20 (2010) 2201–2214.
- [42] G. Li, Z. Tang, *Nanoscale* 6 (2014) 3995–4011.
- [43] C. Zhang, S. Li, T. Wang, G. Wu, X. Ma, J. Gong, *Chem. Commun.* 49 (2013) 10647–10649.
- [44] M.T. Bore, H.N. Pham, E.E. Switzer, T.L. Ward, A. Fukuoaka, A.K. Datye, *J. Phys. Chem. B* 109 (2005) 2873–2880.
- [45] S. Liu, S.-Q. Bai, Y. Zheng, K.W. Shah, M.-Y. Han, *ChemCatChem* 4 (2012) 1462–1484.
- [46] F. Zaera, *Chem. Soc. Rev.* 42 (2013) 2746–2762.
- [47] Y. Chen, H.-R. Chen, J.-L. Shi, *Acc. Chem. Res.* 47 (2013) 125–137.
- [48] M. Pérez-Lorenzo, B. Vaz, V. Salgueiriño, M.A. Correa-Duarte, *Chem. Eur. J.* 19 (2013) 12196–12211.
- [49] T. Mitsudome, K. Kaneda, *ChemCatChem* 5 (2013) 1681–1691.
- [50] C.-C. Lai, W.-C. Chang, W.-L. Hu, Z.M. Wang, M.-C. Lu, Y.-L. Chueh, *Nanoscale* 6 (2014) 4555–4559.
- [51] J. Zhou, G. Tian, Y. Chen, Y. Shi, C. Tian, K. Pan, H. Fu, *Sci. Rep.* 4 (2014) 4027.
- [52] K. Nakatsuka, K. Mori, S. Okada, S. Ikurumi, T. Kamegawa, H. Yamashita, *Chem. Eur. J.* 20 (2014) 8348–8354.
- [53] Y. Long, M. Xie, J. Niu, P. Wang, J. Ma, *Appl. Surf. Sci.* 277 (2013) 288–292.
- [54] J. Qi, W. Lv, G. Zhang, Y. Li, G. Zhang, F. Zhang, X. Fan, *Nanoscale* 5 (2013) 6275–6279.
- [55] R.C. Sekol, X. Li, P. Cohen, G. Doubek, M. Carmo, A.D. Taylor, *Appl. Catal. B: Environ.* 138 (2013) 285–293.
- [56] C. Xu, Y. Yuan, A. Cui, R. Yuan, *J. Mater. Sci.* 48 (2013) 967–973.
- [57] W. Maqbool, E.S. Lee, *Chem. Eng. Technol.* 37 (2014) 995–1001.
- [58] D. Homsí, S. Aouad, C. Gennequin, A. Aboukaïs, E. Abi-Aad, *Int. J. Hydrogen Energy* 39 (2014) 10101–10107.
- [59] J.C. Park, J.U. Bang, J. Lee, C.H. Ko, H. Song, *J. Mater. Chem.* 20 (2010) 1239.
- [60] L. Mo, K.K.M. Leong, S. Kawi, *Catal. Sci. Tech.* 4 (2014) 2107–2114.
- [61] L. Chang-jun, G.M. Richard, A. Michele, *Utilization of Greenhouse Gases*, Am. Chem. Soc., Washington D.C., 2003.
- [62] Y. Kathiraser, S. Kawi, *AIChE J.* 59 (2013) 3874–3885.
- [63] S.D. Davidson, J. Sun, Y. Hong, A.M. Karim, A.K. Datye, Y. Wang, *Catal. Today* 233 (2014) 38–45.



- [64] B. Roy, U. Martinez, K. Loganathan, A.K. Datye, C.A. Leclerc, *Int. J. Hydrogen Energy* 37 (2012) 8143–8153.
- [65] Y. Kathiraser, Z. Wang, S. Kawi, *Environ. Sci. Technol.* 47 (2013) 14510–14517.
- [66] C.-j. Liu, J. Ye, J. Jiang, Y. Pan, *ChemCatChem* 3 (2011) 529–541.
- [67] J.W. Han, C. Kim, J.S. Park, H. Lee, *ChemSusChem* 7 (2014) 451–456.
- [68] Z. Wei, J. Sun, Y. Li, A.K. Datye, Y. Wang, *Chem. Soc. Rev.* 41 (2012) 7994–8008.
- [69] M. Dan, M. Mihet, Z. Tasnadi-Asztalos, A. Imre-Lucaci, G. Katona, M.D. Lazar, *Fuel* 147 (2015) 260–268.
- [70] K. Tomishige, K. Y.-g. Chen, J. Fujimoto, *Catal.* 181 (1999) 91–103.
- [71] M. García-Diéguez, I.S. Pieta, M.C. Herrera, M.A. Larrubia, L.J. Alemany, *J. Catal.* 270 (2010) 136–145.
- [72] Y.-x. Pan, C.-j. Liu, T.S. Wiltowski, Q. Ge, *Catal. Today* 147 (2009) 68–76.
- [73] D. Liu, X.Y. Quek, W.N.E. Cheo, R. Lau, A. Borgna, Y. Yang, *J. Catal.* 266 (2009) 380–390.
- [74] N. Wang, K. Shen, L. Huang, X. Yu, W. Qian, W. Chu, *ACS Catal.* 3 (2013) 1638–1651.
- [75] Y.-H. Wang, H.-M. Liu, B.-Q. Xu, *J. Mol. Catal. A: Chem.* 299 (2009) 44–52.
- [76] L. Yao, T. Shi, Y. Li, J. Zhao, W. Ji, C.-T. Au, *Catal. Today* 164 (2011) 112–118.
- [77] R. Phienlupphon, K. Pinkaew, G. Yang, J. Li, Q. Wei, Y. Yoneyama, T. Vitidsant, N. Tsubaki, *Chem. Eng. J.* 270 (2015) 605–611.
- [78] J.C. Park, H. Song, *Nano Res.* 4 (2011) 33–49.
- [79] T. Zeng, X. Zhang, S. Wang, Y. Ma, H. Niu, Y. Cai, *Chem. Eur. J.* 20 (2014) 6474–6481.
- [80] J. Li, L. Tan, G. Wang, M. Yang, *Nanotechnology* 26 (2015) 095601.
- [81] V. Evangelista, B. Acosta, S. Miridonov, E. Smolentseva, S. Fuentes, A. Simakov, *Appl. Catal. B: Environ.* 166 (2015) 518–528.
- [82] C.-H. Kuo, Y. Tang, L.-Y. Chou, B.T. Sneed, C.N. Brodsky, Z. Zhao, C.-K. Tsung, *J. Am. Chem. Soc.* 134 (2012) 14345–14348.
- [83] X. Du, D. Zhang, R. Gao, L. Huang, L. Shi, J. Zhang, *Chem. Commun.* 49 (2013) 6770–6772.
- [84] G. Zeng, R. Gu, Y. Li, *Int. J. Hydrogen Energy* 38 (2013) 11256–11267.
- [85] G. Zeng, Q. Liu, R. Gu, L. Zhang, Y. Li, *Catal. Today* 178 (2011) 206–213.
- [86] L. Li, S. He, Y. Song, J. Zhao, W. Ji, C.-T. Au, *J. Catal.* 288 (2012) 54–64.
- [87] L. Pelletier, D.D.S. Liu, *Appl. Catal. A: Gen.* 317 (2007) 293–298.
- [88] Y. Chen, W. Zhou, Z. Shao, N. Xu, *Catal. Commun.* 9 (2008) 1418–1425.
- [89] A. Shafiefarhood, N. Galinsky, Y. Huang, Y. Chen, F. Li, *ChemCatChem* 6 (2014) 790–799.
- [90] K.-M. Kang, I.-W. Shim, H.-Y. Kwak, *Fuel Process. Technol.* 92 (2011) 1236–1243.
- [91] X. Zhou, J. Qiao, L. Yang, J. Zhang, *J. Adv. Energy Mater.* 4 (2014) 1301523.
- [92] S.C. Singhal, *WIREs Energy Environ.* 3 (2014) 179–194.
- [93] H. Zhang, L. Chen, J. Zhang, J. Chen, *Energy* 68 (2014) 292–300.
- [94] S. Campanari, G. Manzolini, P. Chiesa, *Appl. Energy* 112 (2013) 772–783.
- [95] L. Adjianto, A. Sampath, A.S. Yu, M. Cargnello, P. Fornasiero, R.J. Gorte, J.M. Vohs, *ACS Catal.* 3 (2013) 1801–1809.
- [96] J. Zhang, X. Zhang, W. Liu, H. Liu, J. Qiu, K.L. Yeung, *J. Power Sources* 246 (2014) 74–83.
- [97] P. Wang, L. Zhou, G. Li, H. Lin, Z. Shao, X. Zhang, B. Yi, *Int. J. Hydrogen Energy* 37 (2012) 2588–2595.
- [98] M. Cargnello, J.J.D. Jaén, J.C.H. Garrido, K. Bakhtmutsky, T. Montini, J.J.C. Gámez, R.J. Gorte, P. Fornasiero, *Science* 337 (2012) 713–717.
- [99] M. Cargnello, M. Grzelczak, B. Rodríguez-González, Z. Syrgiannis, K. Bakhtmutsky, V. La Parola, L.M. Liz-Marzán, R.J. Gorte, M. Prato, P. Fornasiero, *J. Am. Chem. Soc.* 134 (2012) 11760–11766.
- [100] Y. Park, S.K. Kim, D. Pradhan, Y. Sohn, *Chem. Eng. J.* 250 (2014) 25–34.
- [101] N. Singh, D.C. Upham, R.-F. Liu, J. Burk, N. Economou, S. Buratto, H. Metiu, E.W. McFarland, *Langmuir* 30 (2014) 5662–5668.
- [102] D. Li, Y. Zhu, H. Wang, Y. Ding, *Sci. Rep.* 3 (2013) 3015.
- [103] Y. Tang, X. Dai, Z. Yang, L. Pan, W. Chen, D. Ma, Z. Lu, *Phys. Chem. Chem. Phys.* 16 (2014) 7887–7895.
- [104] O.A. Stonkus, L.S. Kibis, O.Yu. Podyacheva, E.M. Slavinskaya, V.I. Zaikovskii, A.H. Hassan, S. Hampel, A. Leonhardt, Z.R. Ismagilov, A.S. Noskov, A.I. Boronin, *ChemCatChem* 6 (2014) 2115–2128.
- [105] Z. Zheng, J. Jia, Z. Zhong, *J. Nanosci. Nanotechnol.* 14 (2014) 6885–6893.
- [106] S. Bonanni, K. Ait-Mansour, W. Harbich, H. Brune, *J. Am. Chem. Soc.* 136 (2014) 8702–8707.
- [107] J. Yang, L. Lukashuk, H. Li, K. Föttinger, G. Rupprechter, U. Schubert, *Catal. Lett.* 144 (2014) 403–412.
- [108] Y. Lou, L. Wang, Z. Zhao, Y. Zhang, Z. Zhang, G. Lu, Y. Guo, Y. Guo, *Appl. Catal. B: Environ.* 146 (2014) 43–49.
- [109] V. Bratan, C. Munteanu, C. Hornoii, F. Papa, N. Ionescu, *React. Kinet. Mech. Catal.* 112 (2014) 51–60.
- [110] Y. Xu, J. Ma, Y. Xu, L. Xu, L. Xu, H. Li, H. Li, *RSC Adv.* 3 (2013) 851–858.
- [111] X. Wang, D. Liu, S. Song, H. Zhang, *J. Am. Chem. Soc.* 135 (2013) 15864–15872.
- [112] Y. Sun, L. Zhang, Y. Wang, P. Chen, S. Xin, H. Jiu, J. Liu, *J. Alloy Compd.* 586 (2014) 441–447.
- [113] J. Zhen, X. Wang, D. Liu, S. Song, Z. Wang, Y. Wang, J. Li, F. Wang, H. Zhang, *Chem. Eur. J.* 20 (2014) 4469–4473.
- [114] N. Yan, Q. Chen, F. Wang, Y. Wang, H. Zhong, L. Hu, *J. Mater. Chem. A* 1 (2013) 637–643.
- [115] Z.-M. Cui, Z. Chen, C.-Y. Cao, L. Jiang, W.-G. Song, *Chem. Commun.* 49 (2013) 2332–2334.
- [116] J. Chen, J. Qi, G. Li, F. Zheng, S. Li, Z. Tang, *Chem. Asian J.* 8 (2013) 694–699.
- [117] B. Smit, T.L.M. Maesen, *Nature* 451 (2008) 671–678.
- [118] H. Yang, Y. Chong, X. Li, H. Ge, W. Fan, J. Wang, *J. Mater. Chem.* 22 (2012) 9069–9076.
- [119] V.R.R. Pendyala, U.M. Graham, G. Jacobs, H.H. Hamdeh, B.H. Davis, *ChemCatChem* 6 (2014) 1952–1960.
- [120] D.-V.N. Vo, V. Arcotumapathy, B. Abdullah, A.A. Adesina, *J. Chem. Tech. Biotechnol.* 88 (2013) 1358–1363.
- [121] H.M. Torres Galvis, K.P. de Jong, *ACS Catal.* 3 (2013) 2130–2149.
- [122] B. Sun, G. Yu, J. Lin, K. Xu, Y. Pei, S. Yan, M. Qiao, K. Fan, X. Zhang, B. Zong, *Catal. Sci. Technol.* 2 (2012) 1625–1629.
- [123] S. Sartipi, J.E. van Dijk, J. Gascon, F. Kapteijn, *Appl. Catal. A: Gen.* 456 (2013) 11–22.
- [124] G. Yang, C. Xing, W. Hirohama, Y. Jin, C. Zeng, Y. Suehiro, T. Wang, Y. Yoneyama, N. Tsubaki, *Catal. Today* 215 (2013) 29–35.
- [125] K. Pinkaew, G. Yang, T. Vitidsant, Y. Jin, C. Zeng, Y. Yoneyama, N. Tsubaki, *Fuel* 111 (2013) 727–732.
- [126] Q. Lin, G. Yang, X. Li, Y. Yoneyama, H. Wan, N. Tsubaki, *ChemCatChem* 5 (2013) 3101–3106.
- [127] G. Vilé, N. Almora-Barrios, S. Mitchell, N. López, J. Pérez-Ramírez, *Chem. Eur. J.* 20 (2014) 5926–5937.
- [128] C. Li, Y. Chen, S. Zhang, J. Zhou, F. Wang, S. He, M. Wei, D.G. Evans, X. Duan, *ChemCatChem* 6 (2014) 824–831.
- [129] G. Petrucci, W. Oberhauser, M. Bartoli, G. Giachi, M. Frediani, E. Passaglia, L. Capozzoli, L. Rosi, *Appl. Catal. A: Gen.* 469 (2014) 132–138.
- [130] Y. Kwon, E. de Jong, S. Raoufmoheghdham, M.T.M. Koper, *ChemSusChem* 6 (2013) 1659–1667.
- [131] A.M. Hengne, A.V. Malawadkar, N.S. Biradar, C.V. Rode, *RSC Adv.* 4 (2014) 9730–9736.
- [132] C.S. Spanjers, J.T. Held, M.J. Jones, D.D. Stanley, R.S. Sim, M.J. Janik, R.M. Rioux, *J. Catal.* 316 (2014) 164–173.
- [133] T. Mitsudome, Y. Takahashi, S. Ichikawa, T. Mizugaki, K. Jitsukawa, K. Kaneda, *Angew. Chem. Int. Ed.* 52 (2013) 1481–1485.
- [134] A.V. Erokhin, E.S. Lokteva, A.Y. Yermakov, D.W. Boukhvalov, K.I. Maslakov, E.V. Golubina, M.A. Uimin, *Carbon* 74 (2014) 291–301.
- [135] M. Zhang, Y. Yang, C. Li, Q. Liu, C.T. Williams, C. Liang, *Catal. Sci. Technol.* 4 (2014) 329–332.
- [136] T. Mitsudome, M. Matoba, T. Mizugaki, K. Jitsukawa, K. Kaneda, *Chem. Eur. J.* 19 (2013) 5255–5258.
- [137] Z. Jin, S. Liu, L. Qin, Z. Liu, Y. Wang, Z. Xie, X. Wang, *Appl. Catal. A: Gen.* 453 (2013) 295–301.
- [138] M.B. Gawande, H. Guo, A.K. Rath, P.S. Branco, Y. Chen, R.S. Varma, D.-L. Peng, *RSC Adv.* 3 (2013) 1050–1054.
- [139] W. Zhang, G. Lu, C. Cui, Y. Liu, S. Li, W. Yan, C. Xing, Y.R. Chi, Y. Yang, F. Huo, *Adv. Mater.* 26 (2014) 4056–4060.
- [140] L. Jia, X. Sun, X. Ye, C. Zou, H. Gu, Y. Huang, G. Niu, D. Zhao, *Microporous Mesoporous Mater.* 176 (2013) 16–24.
- [141] B. Guan, X. Wang, Y. Xiao, Y. Liu, Q. Huo, *Nanoscale* 5 (2013) 2469–2475.
- [142] Y. Yin, R.M. Rioux, C.K. Erdonmez, S. Hughes, G.A. Somorjai, A.P. Alivisatos, *Science* 304 (2004) 711–714.
- [143] F.H. Ribeiro, A.E. Schach Von Wittenau, C.H. Bartholomew, G.A. Somorjai, *Catal. Rev.* 39 (1997) 49–76.